



DEGREE PROJECT IN THE FIELD OF TECHNOLOGY  
VEHICLE ENGINEERING  
AND THE MAIN FIELD OF STUDY  
ELECTRICAL ENGINEERING,  
SECOND CYCLE, 30 CREDITS  
*STOCKHOLM, SWEDEN 2020*

# **Europa's Lyman-Alpha Shadow on Jupiter**

A New Way of Searching for Water Plumes

**JOHAN FERM**



## **Author**

Johan Ferm <johanfer@kth.se>  
Aerospace Engineering  
School of Engineering Sciences  
KTH Royal Institute of Technology

## **Place for Project**

Stockholm, Sweden  
KTH Royal Institute of Technology

## **Examiner**

Tomas Karlsson  
Division of Space and Plasma Physics  
KTH Royal Institute of Technology

## **Supervisor**

Lorenz Roth  
Division of Space and Plasma Physics  
KTH Royal Institute of Technology



# Abstract

Europa is one of the most interesting satellites in the solar system in the search of extra-terrestrial life, as it harbours an interior water ocean under its icy surface. Water vapour in Europa's atmosphere has been previously observed, suggesting water plume eruptions from the surface. These plumes could potentially originate from the subsurface ocean, and as such contain ocean constituents that can be examined in orbit. Two observations of Europa's far-ultraviolet shadow on Jupiter were made by the Hubble Space Telescope in 2018 and 2019. It was observed in Lyman- $\alpha$  (1216 Å), a spectral line of hydrogen. This study investigates the imaged Lyman- $\alpha$  shadow in search of potential plumes at the shadow limb. Examining the shadow instead of the moon itself is a new method of remotely studying the European atmosphere. Forward modelling is applied to create artificial images that are compared to the observations. Any anomalies around the shadow limb are then analysed and evaluated for their statistical significance. Two noteworthy outliers are found at the limb (one on each occasion) corresponding to H<sub>2</sub>O line of sight column densities of  $3.07 \times 10^{17} \text{ cm}^{-2}$  and  $4.72 \times 10^{16} \text{ cm}^{-2}$ , for the 2018 and 2019 observation, respectively. They are not significant however, as they lie within three standard deviations from the expected value ( $< 3\sigma$ ). An upper limit on what column density is detectable in the data is computed, yielding  $6.71 \times 10^{16} \text{ cm}^{-2}$  (using only 2019 data due to a weak signal on the 2018 occasion). A constraint on the maximum possible H<sub>2</sub>O column density at Europa is thus provided. The new method is shown to be useful for the intended purpose and could potentially be applied on other icy moons.

## Keywords

Europa (moon), Jupiter, water, plumes, Solar System, planets, satellites, hydrogen, Lyman-alpha.

# Abstract

Europa är ett av solsystemets mest intressanta objekt i jakten på utomjordiskt liv, då det finns ett hav av vatten under månens isiga yta. Vattenånga har tidigare observerats i Europas atmosfär, vilket kan tyda på vattenplymer som skjuts ut från ytan i kraftiga utbrott. Dessa plymer kan möjligtvis ha sitt ursprung i månens inre hav, de kan därför möjliggöra en analys av havsvattnets beståndsdelar i omloppsbanan. Europas ultravioletta skugga på Jupiter observerades vid två tillfällen 2018 och 2019, av Hubble Space Telescope. Observationerna gjordes i Lyman- $\alpha$  (1216 Å), en spektrallinje hos väte. Denna studie undersöker den avbildade skuggan i Lyman- $\alpha$  för att söka efter potentiella vattenplymer vid skuggans rand. Att undersöka skuggan istället för själva månen är en ny metod för att studera Europas atmosfär genom fjärranalys. Metoden *forward modelling* används för att skapa artificiella bilder, som jämförs med observationerna. Eventuella avvikelser som hittas runt skuggans rand analyseras sedan och deras statistiska signifikans utvärderas. Två anmärkningsvärda avvikelser kan hittas vid randen (en vid varje observationstillfälle), som motsvarar H<sub>2</sub>O-kolumndensiteter på  $3.07 \times 10^{17} \text{ cm}^{-2}$  och  $4.72 \times 10^{16} \text{ cm}^{-2}$ , för 2018-observationen respektive 2019-observationen. Densiteterna är dock inte signifikanta, då de ligger inom tre standardavvikelser från deras förväntade värden ( $< 3\sigma$ ). Istället beräknas en övre gräns för vilken kolumndensitet som kan detekteras i datan, vilket ger  $6.71 \times 10^{16} \text{ cm}^{-2}$  (där endast 2019-data används på grund av en svag signal hos 2018-observationen). Den högsta möjliga H<sub>2</sub>O-kolumndensiteten kan således begränsas. Den nya metoden visar sig vara användbar för det tänkta syftet och kan eventuellt appliceras på andra ismånar.

## Nyckelord

Europa (måne), Jupiter, vatten, polymer, solsystemet, skugga, planeter, satelliter, väte, Lyman-alpha.

# Acknowledgements

I want to thank my supervisor Lorenz Roth for his much appreciated advice and continuous guidance during this past semester of thesis work, introducing me to the subject of planetary science. I also give my thanks to Tomas Karlsson for being the examiner of my thesis.

I would like to express my deepest gratitude to my family and to my girlfriend, Ida. We have all endured great hardships during these years, and I am only able to present this thesis because of their endless love and support.

# Acronyms

<b>CCD</b>	charged coupled device
<b>FOV</b>	field of view
<b>FUV</b>	far-ultraviolet
<b>HST</b>	the Hubble Space Telescope
<b>IPM</b>	interplanetary medium
<b>IPT</b>	Io plasma torus
<b>LOS</b>	line of sight
<b>MAMA</b>	multi-anode microchannel array
<b>PSF</b>	point spread function
<b>STIS</b>	the Space Telescope Imaging Spectrograph
<b>UV</b>	ultraviolet

# List of Figures

1.1	The Galilean moons of Jupiter. . . . .	1
2.1	Cutaway of Europa, showing the possible interior structure. . . . .	6
2.2	Model density and temperature profiles of Jupiter's upper atmosphere, from Ben Jaffel et al. (2007). . . . .	10
2.3	Jupiter Ly- $\alpha$ line profiles of Clarke et al. (1991). . . . .	11
2.4	Jupiter model disk brightness profile by Ben Jaffel et al. (2007). . . . .	12
2.5	Jupiter dayside Ly- $\alpha$ map produced by Melin et al. (2016). . . . .	13
3.1	Illustration of the FUV-MAMA detector setup (modified from Lorenz Roth (2012)). . . . .	15
3.2	Transit image of Io, Callisto and Europa in optical wavelengths. . . . .	16
3.3	Approximate viewing geometries of the observations, as seen from Earth and HST. . . . .	17
3.4	Full exposures of the 2018 and 2019 observations, in detector counts. . . . .	18
3.5	Illustration of the image orientation in STIS relative celestial and Jupiter north. . . . .	20
3.6	The 2018 and 2019 observations in the Ly- $\alpha$ aperture box, with brightness in kR. . . . .	21
3.7	The last 200 seconds of the odr212010 exposure, showing the Jovian limb in close proximity to Europa and its shadow. . . . .	22
3.8	Cut exposures of the observations, that are used for the image modelling and analysis. . . . .	22
3.9	Angular bins for locating the shadow centre, illustrated for odr214010. . . . .	23
3.10	Resulting $\epsilon$ array for odr214010. . . . .	24
3.11	The three primary modelling steps for odr214010. . . . .	25
3.12	A not to scale illustration of H Ly- $\alpha$ sources that may contribute to the observed signal of HST. . . . .	27
3.13	Illustration of model and observation radial profiles. . . . .	28
3.14	Example background surface fits for different order polynomials in $x$ and $y$ , for odr214010. . . . .	29
3.15	Angular bins for analysing the region above the shadow limb. . . . .	32
4.1	Resulting model images that provide the best fits to observations. . . . .	34

4.2	Radial profiles of the observations and models. . . . .	35
4.3	Angular profiles of the observation and model limb. . . . .	36
A.1	Geometry of the Sun-Europa-Jupiter occultation. . . . .	49
A.2	Simplification of the Sun's and Europa's disk geometries. . . . .	50
A.3	Example radial profile of the simplified penumbra model. . . . .	51
B.1	Radial profile bins for the observations. . . . .	52
C.1	Areas excluded from the odr212010 background fit. . . . .	53

## List of Tables

3.1	Observational parameters of the two HST/STIS observations used in this study. . . . .	16
4.1	Properties of the best fit models, displaying the shadow minimum, average Jupiter dayglow, H surface density, if a penumbra is included, chi-squared and upper limit water plume column density. . . . .	33

# Contents

<b>1</b>	<b>Introduction</b>	<b>1</b>
1.1	Background . . . . .	2
1.2	Objective . . . . .	2
1.3	Purpose . . . . .	3
1.4	Methodology . . . . .	3
1.5	Delimitations . . . . .	4
1.6	Outline . . . . .	4
<b>2</b>	<b>Background</b>	<b>5</b>
2.1	Europa . . . . .	5
2.1.1	Geology of Europa . . . . .	6
2.1.2	Europa’s Atmosphere & Water Plumes . . . . .	7
2.2	Jupiter’s Upper Atmosphere in Ly- $\alpha$ . . . . .	9
<b>3</b>	<b>Methods</b>	<b>14</b>
3.1	HST/STIS Observations . . . . .	14
3.2	Image Processing . . . . .	17
3.2.1	Unit Conversion . . . . .	18
3.2.2	Image Orientation . . . . .	19
3.2.3	Limitations on Exposure Time . . . . .	20
3.2.4	Shadow Location . . . . .	22
3.3	Image Modelling & Analysis . . . . .	25
3.3.1	Ly- $\alpha$ Contributions . . . . .	26
3.3.2	Creating Artificial Images . . . . .	27
3.3.3	Shadow Limb Analysis . . . . .	31
<b>4</b>	<b>Results</b>	<b>33</b>
4.1	Model Results . . . . .	33
4.2	Limb Analysis Results . . . . .	35
<b>5</b>	<b>Discussion</b>	<b>37</b>
5.1	Water Plumes . . . . .	37
5.2	Jupiter Background . . . . .	38
5.3	Shadow . . . . .	38

## CONTENTS

---

5.3.1	Elliptic or Circular Shadow . . . . .	39
5.3.2	Shadow Penumbra . . . . .	39
5.4	Hydrogen Corona . . . . .	39
<b>6</b>	<b>Conclusion</b>	<b>41</b>
	<b>References</b>	<b>43</b>

# Chapter 1

## Introduction

Jupiter is placed as the fifth planet from the Sun. Being the most massive planet in our Solar System, with a radius of around 11 Earth radii and a mass of 318 Earth masses, the gas giant and its satellites are some of the most interesting celestial bodies for scientific research. There are currently 79 known moons in the Jovian system (Sheppard, 2018). Out of these, the Galilean moons are the largest, and were the first Jovian moons to be discovered, by Galileo Galilei in 1610. They are displayed in Figure 1.1.



**Figure 1.1:** *The Galilean moons of Jupiter. From left to right: Io, Europa, Ganymede, Callisto. Credit: NASA/JPL/DLR (<https://www.jpl.nasa.gov/spaceimages/details.php?id=PIA01400>, retrieved June 20, 2020).*

The Galilean moons are four heavily irradiated worlds with varying characteristics, such as intense volcanic activity on Io, and the only moon in the Solar System with an intrinsic magnetic field (Ganymede). They are all tidally locked<sup>1</sup>, as they always have the same hemispheres facing Jupiter. In addition, the three innermost moons Io, Europa and Ganymede exhibit an orbital resonance of 1:2:4 (Io, Europa, Ganymede respectively), known as a Laplacian resonance, hence Io's orbit period is half that of Europa's and a quarter of Ganymede's.

---

<sup>1</sup>Europa is not truly locked, but has a slight non-synchronous rotation with a period greater than 10 000 years (Geissler et al., 1998).

Europa has long been of high interest to researchers, due to indications of a liquid water ocean under its icy surface (e.g. Anderson et al., 1998) that could potentially be suitable for life (e.g. Camprubí et al., 2019; Russell et al., 2017). In addition to visits by various spacecraft, ground-based and space telescopes provide continuous remote observations that help research the moon’s habitability.

Hydrogen, the most abundant element in the Universe, can be used to investigate celestial bodies through remote sensing. Its spectral emissions are used for determining atmospheric and surface compositions. The Lyman- $\alpha$  (Ly- $\alpha$ ) line is one such spectral line, which is created through de-excitation of atomic hydrogen (H), when the electron falls from the  $n = 2$  orbital to the  $n = 1$  orbital. The resulting photon is emitted in the far-ultraviolet (FUV) spectrum, at 1215.67 Å.

Ly- $\alpha$  emissions that are produced by hydrogen in the Solar System originate from the Sun, the interplanetary medium (IPM) and planetary bodies, including Europa. The basic state transition in H that produces Ly- $\alpha$  is very common. Together with high abundances of H, particularly in the Sun, high photon fluxes at 1215.67 Å are generated. In addition to measuring H abundance, observing the emission/absorption of these high fluxes at this wavelength around Europa is a useful way of probing the moon for signs of water that may come from the subsurface ocean. This is because water molecules have a sufficiently high absorption cross section around 1215.67 Å, while also likely being present on Europa in adequate abundances to enable detection.

## 1.1 Background

Local enhancements of water vapour in Europa’s thin atmosphere have previously been detected by e.g. Roth et al. (2014b) and Sparks et al. (2016), by observing the moon in Ly- $\alpha$  and other ultraviolet (UV) wavelengths. The detections (which were made at the disk limb, as seen from Earth) can be associated to the presence of potential water plumes that erupt from the surface. The plume water may originate from the subsurface ocean, hence it can provide clues to the ocean’s composition.

If more evidence of plumes emanating from Europa were to be found, it would motivate sending a probe to perform *in-situ* measurements of the plume constituents, as this could help uncover Europa’s capabilities of supporting life (Camprubí et al., 2019; Prockter et al., 2014; Russell et al., 2017). This would be less costly and more feasible than reaching the subsurface ocean through the ice.

## 1.2 Objective

On two occasions in 2018 and 2019, the Space Telescope Imaging Spectrograph (STIS) on board the Hubble Space Telescope (HST) observed Europa in transit across the Jovian

disk. The observations were made in FUV (including Ly- $\alpha$ ), close to Jupiter opposition<sup>2</sup>. This viewing geometry also managed to capture Europa's Ly- $\alpha$  shadow on Jupiter in the process. If plumes were present at the times of observation, an analysis of the recorded images can possibly provide further evidence that motivates a mission to the icy moon.

As solar Ly- $\alpha$  radiation could be absorbed by plumes, the absence of light after passing through them should be replicated in the shadow. It should therefore be possible to also study the FUV shadow, as visible in the two observations from 2018 and 2019, in search of water plumes.

The objective of this study is thus to investigate the morphology of Europa's Ly- $\alpha$  shadow on Jupiter, to look for anomalies around the shadow limb. This is done by analysing the images in the two observations. This method of searching for plumes is a new way of remotely studying the European atmosphere, as previous observations to search for plumes have only been made of the moon itself.

### 1.3 Purpose

The purpose of the study is to investigate potential plume activity on Europa, but also to evaluate if this new method of examining the shadow in Ly- $\alpha$  is useful for studying the atmosphere, on Europa as well as on other icy moons.

### 1.4 Methodology

To analyse astronomical images, several different documented methods are available. One can apply different filters, transforms and operators to reduce noise, detect edges and shapes, or segment the image into different classes (Starck et al., 2006). One may try statistical methods such as the entropy concept, or use deconvolution to deblur images (Misra et al., 2018; Starck et al., 2006).

Although these and many other methods are applicable to the wide field of astronomy, their use is often limited to certain types of observations. For studies that have similar observational conditions as in this study, in particular Roth et al. (2014b), Roth et al. (2017), Sparks et al. (2016) and Alday et al. (2017), another method for analysis is common. They all use the approach of forward modelling, where artificial images are created of the observations and their statistical properties are compared in order to draw conclusions.

Hence, following the common practice, the forward modelling method is used in this study, both for the purpose of using a method that is shown to have adequate construct validity (the results reflect what actually was intended to be investigated, i.e. abundances

---

<sup>2</sup>Opposition is when two celestial bodies are aligned, with Earth in between, in this case between the Sun and Jupiter.

of hydrogen and possibly water) and to make the results comparable with those of the referenced studies.

## 1.5 Delimitations

Some general delimitations are placed on the study, so that its scope may be narrowed to cover those aspects of the observations that are essential for an adequate analysis.

Normally, Europa itself is observed when investigating its properties, and artificial images that emulate the moon are required for the forward modelling. This will not be done here, as modelling of the moon is considered non-essential to the shadow's analysis. Only the tenuous atmosphere at Europa is modelled when required.

Otherwise it is only the shadow of the moon and accompanying atmosphere, produced on Jupiter, that is analysed. Further, any variations in the surrounding Ly- $\alpha$  environment, by e.g. the Io gas torus, are neglected, as their ability to influence the images beyond what models can reproduce is assumed negligible.

Other sources that may produce local variations in Ly- $\alpha$  emission are also dismissed, since their physical processes are considered too complex to model here. Such sources are for example Jupiter aurora (West, 2014).

In summary, only aspects that are closely related to the properties of Europa's Ly- $\alpha$  shadow and the HST observations are considered. Using a simple model with few variable aspects may however still have difficulty with performing an adequate analysis. The main limitation of the two observations from 2018 and 2019 is their image quality. The small amount of photons that were recorded by STIS resulted in images with significant noise. The noisiness makes any analysis of small spatial variations suffer (such as signs of water plumes in the shadow), as the statistical uncertainty is prominent and can mask them well.

## 1.6 Outline

The report is structured as follows. Chapter 2 reviews what is currently known about Europa and Jupiter's atmosphere, that may influence the underlying assumptions of the observations. Chapter 3 deals with the overall method of image processing, forward modelling and image analysis, and Chapter 4 then presents the results from the analysis. Chapter 5 discusses the results and a conclusion of the study is finally given in Chapter 6.

# Chapter 2

## Background

To model Europa's shadow, some background knowledge on the moon and on Jupiter needs to be provided. This chapter therefore presents fundamental characteristics of Europa's interior and exterior processes, as well as Jupiter's upper atmosphere in Ly- $\alpha$ , that govern the modelling assumptions.

### 2.1 Europa

Europa has a mass of approximately  $4.8 \times 10^{24}$  kg with a mean radius of 1 560.8 km (=  $1 R_E$ ), which is about 90% of the radius of Earth's Moon. It has a nearly circular orbit around Jupiter at a mean distance of 9.4 Jupiter radii ( $R_J^1$ ), with an eccentricity of 0.009, an inclination of  $0.47^\circ$  and with an orbital period of 3.55 days (8.58 Jupiter days<sup>2</sup>). Jupiter's magnetosphere extends 45–100  $R_J$  on the dayside and thousands of  $R_J$  in the magnetotail. This makes Europa always reside in Jupiter's magnetospheric environment, specifically in its inner region ( $< 10 R_J$ ), which is also the location of the Io plasma torus (IPT) that holds the majority of the magnetospheric plasma, consisting of heavy sulfur and oxygen ions.

Due to the plasma being frozen to the magnetic field lines, it co-rotates with Jupiter at a period of 9 h 55 min, which is significantly faster than Europa. With the moon being essentially tidally locked, its trailing hemisphere is thus constantly irradiated by charged particles. The heavy plasma of the IPT also generates a particularly strong current in the magnetosphere equatorial region, which is confined as a thin current sheet. Due to the current sheet being oriented along Jupiter's magnetic equator, with a slight normal tilt to Jupiter's rotational pole ( $\sim 10^\circ$ ), Europa's low inclination orbit largely coincides with the current sheet, further increasing the bombardment of charged particles.

---

<sup>1</sup>  $1 R_J \approx 69\,911$  km.

<sup>2</sup> One Jupiter day is approximately 9 h 55 min.

### 2.1.1 Geology of Europa

Europa has a surface of water ice and a differentiated interior (Greeley et al., 2004; Pappalardo et al., 1999; Prockter et al., 2014). Using measurement data from the Galileo spacecraft, Anderson et al. (1998) derived the existence of a metallic core with a rocky mantle, surrounded by an icy-liquid water shell, approximately 100 km thick (Pappalardo, 2013). Further evidence of a liquid subsurface ocean has been reported, through the existence of an induced magnetic field which requires a saline composition (Khurana et al., 1998; Kivelson et al., 2000; Zimmer et al., 2000), through observations of mobile surface terrain (Carr et al., 1998), as well as Europa's non-synchronous rotation (Geissler et al., 1998) indicating an internal lubrication between the surface and core by a ductile or liquid material. A cutaway of the possible interior structure is visible in Figure 2.1.

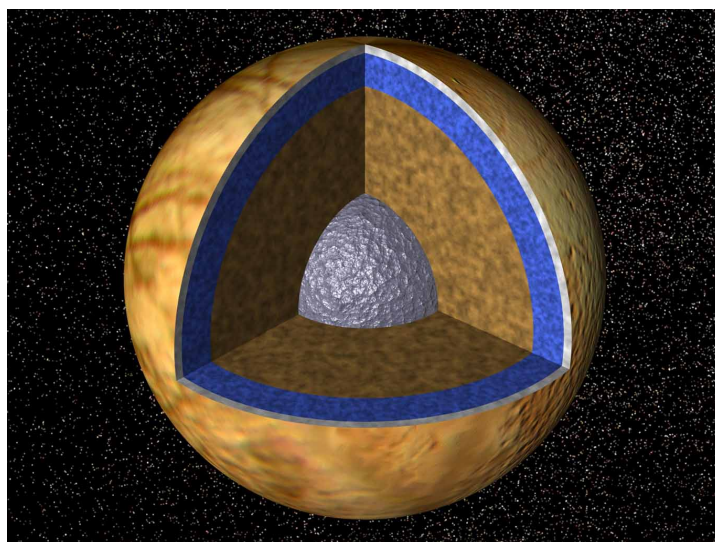


**Figure 2.1:** *Cutaway of Europa, showing the possible interior structure. A metallic core resides in the centre, with a rocky mantle, that is surrounded by a subsurface ocean. A water ice lithosphere serves as the moon's surface. Credit: NASA/JPL (<https://www.jpl.nasa.gov/spaceimages/details.php?id=PIA01130>, retrieved June 20, 2020).*

The surface exhibits some of the geologically youngest features in the solar system (e.g. Pappalardo et al., 1999). Ice fractures of ridges and bands, as well as impact craters, are overlaid by smoother plains and chaotic terrain. Tidal forces due to the slight eccentricity of Europa's orbit are thought to drive the geologic activity, resulting in the changing surface and preventing the ocean from freezing (e.g. Schubert et al., 2004). Endogenic water surfacing processes are suggested to cause surface rejuvenation (Fagents, 2003; Fagents et al., 2000; Greeley et al., 2004; Pappalardo et al., 1999). It is also argued by Kattenhorn et al. (2014) that plate tectonics are driving the recycling of material and that a thinner plate system is located above warmer convective ice.

Several mechanisms are suggested for water resurfacing. Amongst them are diapirs, buoyant pockets of ascending warm ice (Fagents, 2003; Mitri et al., 2008; Pappalardo et al., 1999), as well as tidal flexing along fault lines that squeezes ice melt from fractures

(Pappalardo, 2013). Cryovolcanism, i.e. eruption of water and other volatiles due to subsurface overpressure, is also proposed (Fagents et al., 2000; Noviello et al., 2019; Pappalardo, 2013; Pappalardo et al., 1999). Possible sources of cryovolcanic extrusion are thought to be reservoirs of fluid water that reside in harder ice lithosphere and cracks penetrating to the subsurface ocean, enabling ascent of warmer water (Fagents, 2003; Fagents et al., 2000; Lesage et al., 2020; Pappalardo, 2013; Pappalardo et al., 1999).

Observations of transient water plumes emanating from Europa have been reported by Roth et al. (2014b), Sparks et al. (2016) and Sparks et al. (2017). These tentative plumes might be associated to explosive cryovolcanic eruptions. However, for fractures penetrating to a continuous ocean, plume eruptions of pure water are not possible (Manga et al., 2007), as the water density is greater than what the generated ocean pressure can push upwards. Volatile compounds, such as CO, N<sub>2</sub>, CH<sub>4</sub> and H<sub>2</sub>, would also be needed for sufficient pressure generation and bulk density decrease as Pappalardo et al. (1999) describes and as Neveu et al. (2015) proposes for similar icy bodies in the solar system. Non-ice contaminants are also possible for increasing the bulk density of ice, decreasing the required water pressure for ascent (Fagents, 2003; Pappalardo et al., 1999). Localised liquid reservoirs are another possibility of eruptions, as pressure builds up when water freezes and increases in surrounding volume (Lesage et al., 2020; Pappalardo et al., 1999).

## 2.1.2 Europa's Atmosphere & Water Plumes

Europa has a tenuous atmosphere that is generated mainly by surface sputtering, i.e. the bombardment of energetic ions from the plasma environment, ejecting particles (mainly ice) into space (e.g. Greeley et al., 2004; Prockter et al., 2014). Other mechanisms include ionization and dissociation by electron-impact, UV-photon and photo-electron impact and ice sublimation (Prockter et al., 2014; Shematovich et al., 2005; Smyth et al., 2006). The atmospheric species are mainly products of sputtered H<sub>2</sub>O and other trace elements. Some reported species are O<sub>2</sub> (Hall et al., 1998; Hall et al., 1995), H (e.g. Roth et al., 2017), H<sub>2</sub> (e.g. Mauk et al., 2003), OH and O (Smyth et al., 2006), Na (Brown et al., 1996), K (Brown, 2001), as well as predicted abundances of SO<sub>2</sub> and CO<sub>2</sub> (Cassidy et al., 2009). Lighter elements such as O, H and H<sub>2</sub> also escape the atmosphere and accumulate in a neutral gas torus along Europa's orbit (e.g. Hansen et al., 2005; Smith et al., 2019; Smyth et al., 2006).

The most abundant species in the European atmosphere is molecular oxygen (O<sub>2</sub>), which is dominant at lower altitudes since it does not escape and is not considerably affected by the environment through reactions, as other elements are (Prockter et al., 2014; Roth et al., 2016; Smyth et al., 2006). Upper limits on column densities were reported by Hall et al. (1998) and Roth et al. (2016) to be  $\sim 10^{14}$  cm<sup>-2</sup>, with a surface pressure  $10^{-11}$  that of Earth's at sea level (Hall et al., 1995). Cassidy et al. (2007) also predicted an O<sub>2</sub> surface number density of  $\sim 5 \times 10^8$  cm<sup>-3</sup>. H<sub>2</sub> is dominant at higher altitudes, with estimated column densities of  $10^{13}$  cm<sup>-2</sup> (Smyth et al., 2006). A fast escaping atomic hydrogen corona was also detected by Roth et al. (2017), where surface densities were

constrained to roughly  $2 \times 10^3 \text{ cm}^{-3}$ , which agrees with results from Smyth et al. (2006) and corresponds to a maximum column density of  $\sim 10^{12} \text{ cm}^{-2}$ .

### Water Plumes

Observations of atmospheric constituents (that may be due to outgassing of water vapour) such as those of Hall et al. (1995), Hall et al. (1998) and Roth et al. (2014b) were made of their ultraviolet airglow, i.e. auroral emission, produced by electron impact dissociative excitation. In Roth et al. (2014b) they reported a local enhancement of H and O emission at the limb of Europa, consistent with two water plumes approximately 200 km high, with associated column densities of  $10^{16} \text{ cm}^{-2}$ , though there is uncertainty in the derived plume height of  $\sim 100$  km. This estimated height is greater than what models in Fagents et al. (2000) conclude, where plumes from explosive cryovolcanic eruptions are constrained to heights of up to 25 km, which coincides with model constraints from Quick et al. (2013) of 2.5–26 km.

Eruption velocities of 81–261 m/s in Quick et al. (2013) are also more in line with those of Fagents et al. (2000) (30–250 m/s), than the suggested 700 m/s in Roth et al. (2014b). Sparks et al. (2016) also reported plume detections on three occasions in early 2014 with column densities of  $\sim 10^{17} \text{ cm}^{-2}$ , by observing the attenuation of Jupiter’s UV dayglow in Europa’s atmosphere. Further evidence for plumes were given by Jia et al. (2018) through magnetic field- and plasma wave measurements by the Galileo spacecraft at a close encounter with the moon, providing a detection that is independent of the commonly used observational method.

### Plume Frequency

The frequency of plume eruptions on Europa is important to know when assessing the feasibility for performing successful *in-situ* missions or observational campaigns. No unambiguous evidence for plumes has been reported to the degree of which the plumes at Enceladus has been (Nimmo et al., 2014). Hence, it is difficult to navigate published data to determine whether Europa’s plumes are somewhat recurrent or occur more sporadically. The data can be viewed more as indicators for plumes, with significant uncertainty still present. Only one 2012 observation out of three in Roth et al. (2014b) showed signs of water plumes. Follow up observations on two occasions in 2014 in Roth et al. (2014a) did not detect any plumes, indicating transient behaviour and showing that the dependency on the orbital position is not a sufficient condition for plume activity.

Neither Roth et al. (2017) did find any significant anomalies attributable to plumes, in six observations (late 2014–early 2015) of Europa in transit over Jupiter’s disk. For the obtained signal-to-noise in their data,  $\text{H}_2\text{O}$  column densities higher than  $2 \times 10^{17} \text{ cm}^{-2}$  would be significant, meaning that they can exclude  $\text{H}_2\text{O}$  column densities present in two out of three images associated with plumes in Sparks et al. (2016), but cannot exclude column densities of  $0.7 \times 10^{17} \text{ cm}^{-2}$  and  $1.5 \times 10^{16} \text{ cm}^{-2}$  associated with a third detection in Sparks et al. (2016) and the detection in Roth et al. (2014b), respectively.

Considering the limitations of the observing technology used for detection, and the sparse number of plume detections reported from the described observations, some indication can be given that plumes on Europa are rare events. One detection in March 2014 from Sparks et al. (2016) was suggested to be linked to another detection in the same location in 2016 by Sparks et al. (2017), giving the possibility of a consistently active source. However, Giono et al. (2020) analysed the data of Sparks et al. (2016) and argues that all the detections may be attributed to noise, making the notion of a continuously active vent less likely.

The rarity of anomalies also occurs in Paganini et al. (2020), where a significant water mass was measured on one occasion in 2016, out of 17 separate dates. The measurement was made through infrared observations of Europa’s leading hemisphere and corresponds to an H<sub>2</sub>O column density of  $\sim 10^{15}$  cm<sup>-2</sup>, and Paganini et al. suggest that water outgassing is a localized and rare occurrence.

In summary, the indications that plumes are rare and isolated events are commonly suggested, as described. The apparent range in column density is quite large, spanning  $10^{15}$ – $10^{17}$  cm<sup>-2</sup> (Paganini et al., 2020; Roth et al., 2014b; Sparks et al., 2016). Viewing this study in light of the others mentioned, the possibility of detecting any anomalies here is relatively small, considering only two observations are analysed, while e.g. Sparks et al. (2016) had ten datasets and only three of them gave possible plume detections. However, this study is also the first ever analysis of the Ly- $\alpha$  shadow of an icy moon on Jupiter, thus it serves as a first test for how useful such observations are for the intended purpose of plume detection.

## 2.2 Jupiter’s Upper Atmosphere in Ly- $\alpha$

In this study, the Jovian disk serves as the background in the Ly- $\alpha$  observations. Hydrogen Ly- $\alpha$  emissions in the upper atmosphere of a giant planet like Jupiter is generated by resonant photon scattering of H, by Rayleigh scattering of H<sub>2</sub>, or by excitation by energetic electrons or chemical reactions. This section thus reviews current knowledge on the Jovian atmospheric composition and profile in Ly- $\alpha$ , to better understand the observations.

Jupiter’s atmosphere roughly consists of 90% H<sub>2</sub>, 10% He and other minor species such as H, H<sub>2</sub>O, NH<sub>3</sub>, and different hydrocarbons (Atreya et al., 2003; Atreya et al., 1999). Much of the atomic hydrogen is believed to be produced in the auroral regions, which is then transported to lower latitudes (Yelle et al., 2004). In the upper atmosphere, H becomes more dominant with increasing altitude, specifically in the thermosphere and ionosphere<sup>3</sup> (Moses et al., 2004). A model number density profile of common atmospheric species is displayed in Figure 2.2, where H is dominant at high altitudes.

The main production mechanism of H Ly- $\alpha$  in the upper atmosphere is solar resonant scattering (e.g. Clarke et al., 1990; Melin et al., 2016; Skinner et al., 1988; Yelle et al.,

---

<sup>3</sup>The same terminology is used for Jupiter’s atmospheric layers, as for Earth’s atmosphere.

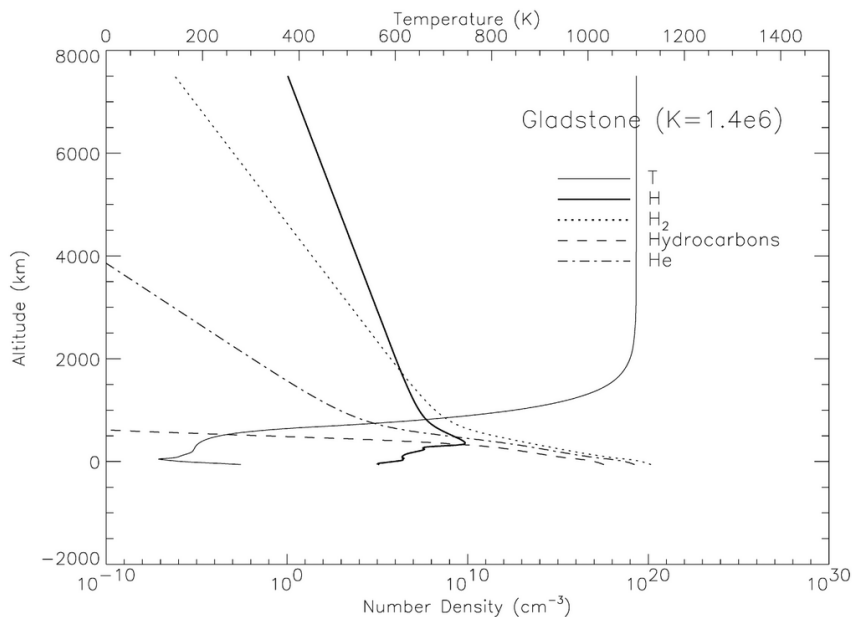


**Figure 2.2:** Model density and temperature profiles of Jupiter’s upper atmosphere, from Ben Jaffel et al. (2007). The used model, with an eddy diffusion coefficient of  $K = 1.4 \times 10^6 \text{ cm}^2/\text{s}$ , is created by Gladstone et al. (1996) and is a standard model atmosphere of Jupiter. The eddy diffusion coefficient is a measure of how well atmospheric substances mix due to eddy motion. The zero-level in altitude corresponds to a 1-bar pressure level.

2004;). Since the analysis of the observations focuses on Europa’s ultraviolet shadow on the Jupiter dayglow, the scattering processes in the upper atmosphere are briefly examined. These processes could affect the properties of the shadow, for example whether it is similar to a shadow on a solid surface, or whether there are 3D-effects.

Models indicate that Ly- $\alpha$  scattering becomes prominent from the thermosphere and upwards (Moses et al., 2004). Ben Jaffel et al. (2007) predicts the scattering H layer thickness in the uppermost atmosphere to be 1700 km at the poles and 3900 km in equatorial regions, where the thickness depends on H abundance and on how Ly- $\alpha$  radiation scatters in the H corona across its spectral profile. Ly- $\alpha$  radiation is generally not a discrete wavelength, but a wider emission line that is distributed within a few Å around the peak at 1215.67 Å, due to non-zero temperatures in H atoms and other system imperfections. As such the line’s spectral profile contains a core (including the peak) and line wings.

The Ly- $\alpha$  line core is optically thick, hence this part of the emission originates from the top of the H corona, while the optically thin line wings originate from greater depths, down to the homopause at 380 km above the 1-bar level (Ben Jaffel et al., 2007, visible as the H density peak in Figure 2.2). Line profiles at different locations on Jupiter’s disk from Clarke et al. (1991) are presented in Figure 2.3. A broadening of the profile is visible at the disk limb, including a decrease in the line core intensity compared to the profile towards the disk centre. This agrees with model profiles of Ben Jaffel et al. (2007), hence the dayglow at the limb could be assumed to be more dominated by line wing scattering,

originating from a thicker H layer.

A model disk brightness profile from Ben Jaffel et al. (2007) is displayed in Figure 2.4, which illustrates that the optically thick line core dominates the scattering across most of the disk, except at the limb. For the FUV shadow, this would mean that Ly- $\alpha$  originates from a shallow H layer for almost the entire disk.

The shadow is the volume of space behind Europa that is blocked from incident solar Ly- $\alpha$ . On Jupiter, the shadow is an atmospheric column that scatters less light than its surroundings. As such, for the shallow H layer, the shadow could be considered a two-dimensional silhouette of Europa (i.e. a flat shadow projection). At the limb, the scattering from a thicker H layer would instead produce an extended shadow volume, with a more three-dimensional structure (i.e. a volumetric shadow projection).

The apparent shadow structure is also affected by viewing geometry. A small phase angle<sup>4</sup> would align the shadow column with the observer, reducing the effects of varying scattering layer thickness, and making it appear more two-dimensional on the entire Jovian disk.

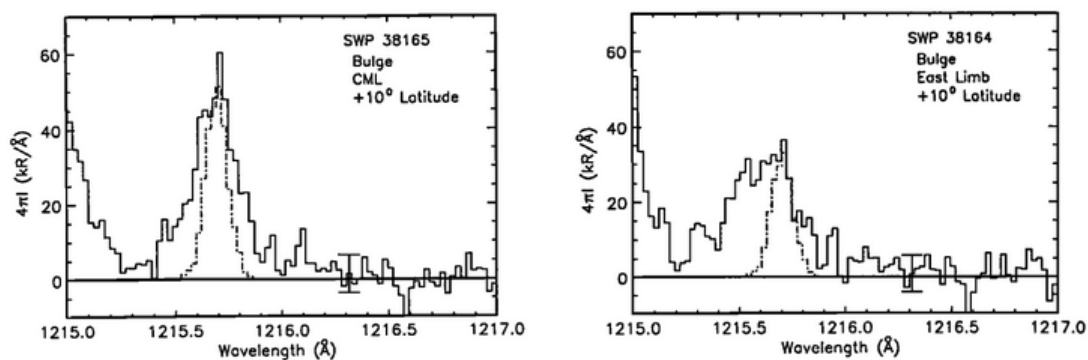


**Figure 2.3:** *Jupiter Ly- $\alpha$  line profiles of Clarke et al. (1991) (only displaying two of six panels of their figure). The profiles are of the hydrogen bulge at  $10^\circ$ N latitude, at the Jovian disk centre (left panel) and at the east limb (right panel), where solid lines are observations and dashed lines are the instrument response to the monochromatic emission at the rest wavelength of Jupiter. A clear line core decrease is visible at the limb, compared to the disk centre, while the line wing contribution increases. The bulge region also contributes to a general line broadening.*

Spatial and temporal variations of the Ly- $\alpha$  dayglow are also important to understand when investigating the Jovian background in the observations. Jupiter exhibits a region of consistently higher emission, known as the hydrogen (or Ly- $\alpha$ ) bulge (e.g. Sandel et al., 1980). This feature is fixed in the system-III coordinate system<sup>5</sup> and is located around the magnetosphere equator (e.g. Dessler et al., 1981; Melin et al., 2016), therefore the spatial Ly- $\alpha$  profile can be divided into a bulge and non-bulge region. Melin et

<sup>4</sup>Phase angle is the angle between incident solar radiation onto an object and the reflected radiation to the observer.

<sup>5</sup>The system-III frame co-rotates with the magnetic field.

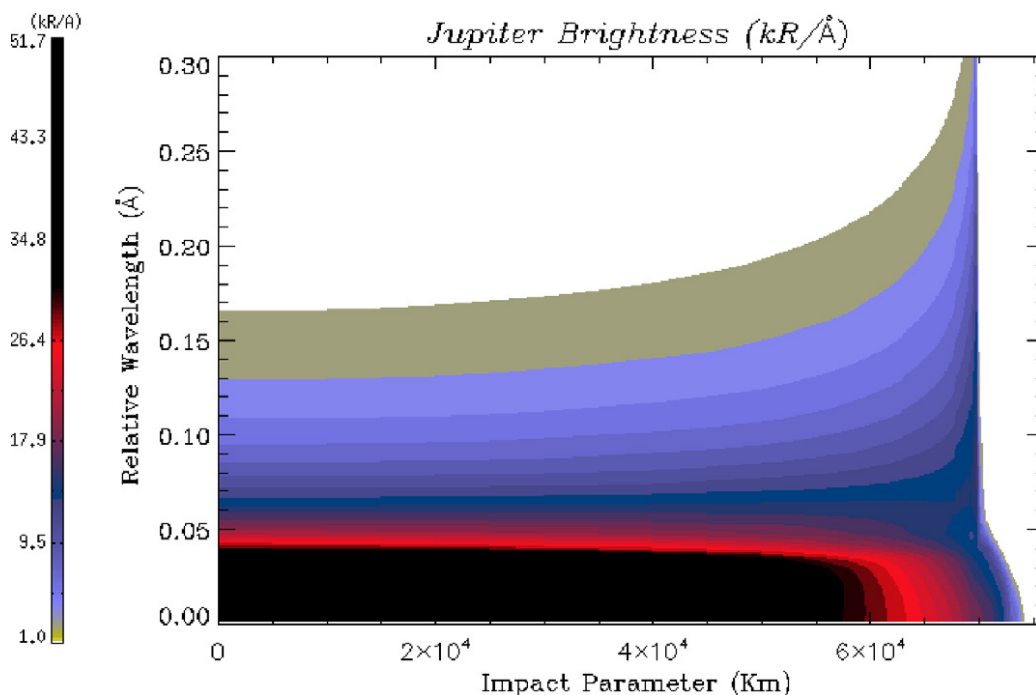


**Figure 2.4:** *Jupiter model disk brightness profile (from the Jovian disk centre to the limb) by Ben Jaffel et al. (2007). The color scheme represents the photometric brightness per  $\text{\AA}$  of the Jovian Ly- $\alpha$  line profile. The y-axis displays  $\Delta\lambda$  from 1215.67  $\text{\AA}$  and the x-axis displays the radial distance from Jupiter’s centre (here denoted Impact Parameter). The profile shows that the Ly- $\alpha$  line core dominates the emissions on most of Jupiter’s disk, while the line wings dominate at the limb, around  $(6.5\text{--}7) \times 10^4$  km.*

al. (2016) produced detailed maps of Jupiter’s Ly- $\alpha$  emissions of both day-and nightside from Cassini flyby data in 2000–2001. Figure 2.5 displays the dayside map, where the H bulge is visible around  $100^\circ$  longitude. The clear banding structure of Jupiter’s clouds in visible wavelengths is not present in Ly- $\alpha$ , rather the emissions have smoother transitions from bulge to non-bulge regions, and the brightness is generally higher near the equator and fainter near the poles.

The hydrogen bulge has consistently been present in the planet’s Ly- $\alpha$  emissions over at least 20 years of observations. The source of the feature is not known, though it has been suggested to be a result of a local increase in electron recombination of  $H_3^+$  into H (Melin et al., 2016). A peak bulge intensity of 22 kR was reported by Melin et al. (2016), which is consistent with previous observations (Clarke et al., 1980; Gladstone et al., 2004; Sandel et al., 1980; Skinner et al., 1988), with variations on shorter timescales of days to months, often more variable than the non-bulge region (Melin et al., 2016; Skinner et al., 1988). The non-bulge region varies spatially from 10 to 20 kR (Melin et al., 2016).

The dayglow is overall highly dependent on the solar Ly- $\alpha$  flux, due to the dominant mechanism for emission being solar resonant scattering by H atoms (Clarke et al., 1990; Clarke et al., 1991; Clarke et al., 1980; Melin et al., 2016). As such the dayglow follows the solar cycle, and it can be assumed that this is the case for the observations analysed in this study. The observations were made during a solar minimum (few sunspots), while

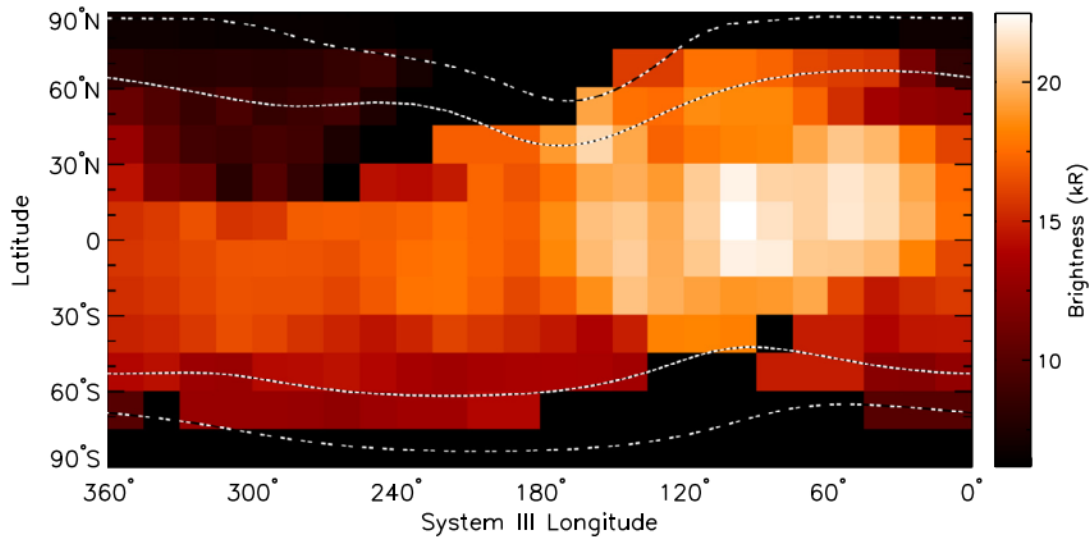


**Figure 2.5:** *Jupiter dayside Ly- $\alpha$  map produced by Melin et al. (2016), using Cassini flyby data. The brighter hydrogen bulge region is visible at  $\sim 100^\circ$  system-III longitude.*

the images in the Melin et al. (2016) maps were recorded during a solar maximum, at  $\sim 40\%$  higher flux (LASP, 2020). The Ly- $\alpha$  background is therefore likely lower in the 2018 and 2019 images than in the Melin et al. maps.

# Chapter 3

## Methods

This chapter describes the method that is used for analysing the obtained images in search of water plumes. The observations of HST/STIS and the provided data are further explained, the images are processed and prepared for performing the forward modelling.

### 3.1 HST/STIS Observations

The observations in this study were made with STIS, which consists of three detector arrays that provide spatially and spectrally resolved images in both optical and ultraviolet wavelengths; one charged coupled device (CCD) detector operating in wavelengths of 2000–11 000 Å, a Cs<sub>2</sub> Te multi-anode microchannel array (MAMA) detector operating in the near-ultraviolet range (1 600–3 100 Å) and a CsI MAMA detector operating in FUV (1 150–1 700 Å). The CCD detector has a field of view (FOV) of 52'' × 52'' and the two MAMA detectors both have 25'' × 25'' fields of view, all detectors provide 1024 × 1024 pixel resolution images.

The FUV-MAMA detector was used for the observations, with a 6'' × 6'' aperture wide slit (here also denoted as aperture box), and the G140L grating. (Details on STIS, its apertures and gratings are available in Riley et al. (2019)). With this configuration operating in spectroscopic mode, images that are both spectrally and spatially resolved can be obtained. The dominant line emissions that are brighter than the remaining continuum passing through the grating are manifested as spatial images in two dimensions according to the aperture shape, in this case as 6'' × 6'' images. The G140L grating passes wavelengths of 1 150–1 700 Å, where for the observations in question, the dominant line is Ly- $\alpha$  (1 215.67 Å).

Figure 3.1 illustrates how STIS produces images in the spectroscopic mode. Incident light is scattered by the grating into separate wavelengths along the dispersion axis, while maintaining spatial information along the cross-dispersion axis. For the dominant Ly- $\alpha$ , spatial information is also preserved along the dispersion axis, producing a monochromatic 2D-image as passed through the aperture box. Hence both spatial and

spectral information is maintained along the dispersion axis. The disks of Europa and its shadow fit well within the slit, providing adequate views of the surrounding Jupiter H dayglow, and enabling background analysis.

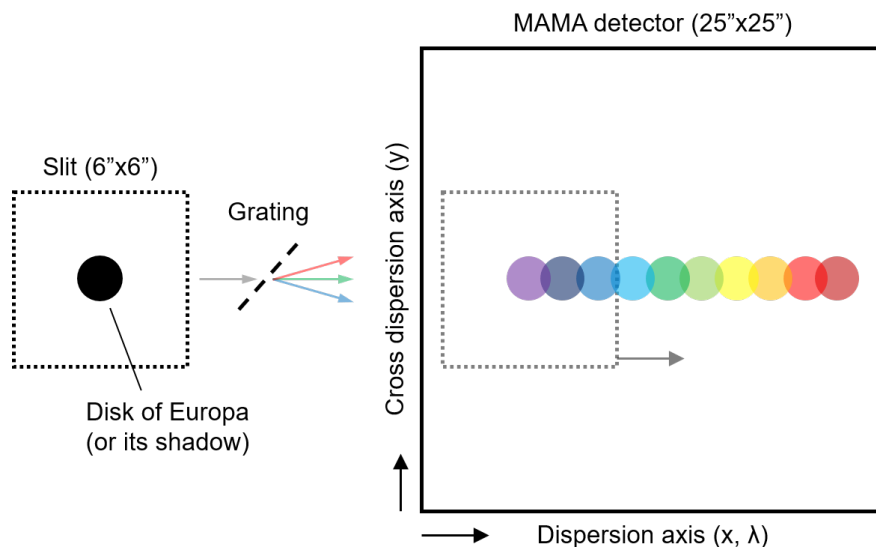


**Figure 3.1:** *Illustration of the FUV-MAMA detector setup (modified from Lorenz Roth (2012)).*

In addition to storing spectral and spatial information in a single image, STIS also has the capability to save the time stamp associated to every photon event that is recorded on the detector throughout an exposure. This recording mode is called TIME-TAG and is used in the observations of this study. The exposures can thus be cut and enables a temporal view of the shadow's transit across the jovian disk.

Data products from STIS are calibrated to different extents that depend on the selected detector and imaging mode used. The end user retrieves data products with different file extensions representing the extent of their calibration. In this study the data files have *flt* (flat-fielded science) extensions, meaning that raw data from the FUV-MAMA detector has gone through an intermediate calibration process, including a pixel quality check, dark-current subtraction, and flat-field correction (Sohn et al., 2019).

An *flt*-file contains three data arrays and several file headers. The headers give useful information for further image analysis, such as telescope orientation, date, exposure time, and references to additional calibration files. The arrays are specified as one science array containing the detector pixel counts  $C(x, y)$ , which is related to the measured flux, one array with the statistical errors for each pixel  $\sigma_0(x, y)$ , and one array containing pixel quality information.

The two observations from 2018 and 2019 were made of Europa in transit across the jovian disk, close to Jupiter opposition, capturing the European shadow on Jupiter in the process. Figure 3.2 shows one of these transits along with other Galilean moons, captured in optical wavelengths with HST.

Table 3.1 provides information about the observations that is relevant for image analysis

of the shadow, since that is what is of interest here. The tabulated exposure times are the maximum time intervals available. These times are modified in Section 3.2 according to changing viewing geometry throughout the exposures.

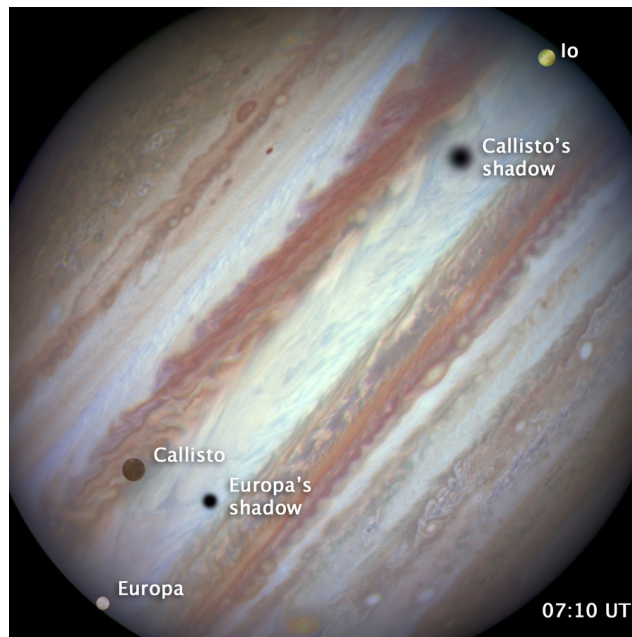


**Figure 3.2:** *Transit image of Io, Callisto and Europa in optical wavelengths. The shadows of Europa and Callisto are also visible on Jupiter, showing similar viewing geometries as in this study’s observations. Credit: NASA, ESA, and the Hubble Heritage Team (<https://apod.nasa.gov/apod/ap150206.html>, retrieved July 2, 2020).*

**Table 3.1:** *Observational parameters of the two HST/STIS observations used in this study.*

HST campaign ID	Dataset	Date	Start time (UTC)	Exposure time [s]	Europa (shadow) diameter ["]	Spatial resolution [km/pixel]	Phase angle [°]
15419	odr212010	2018-05-05	23:52:17	1574.198	0.9793 (0.9793)	78.54	0.66
	odr214010	2019-05-14	04:15:48	2166.200	0.9786 (—)	78.60	5.39

Figure 3.3 shows approximate viewing geometries at the observations’ start times. The FOV of the HST/STIS aperture is marked to give an idea of the images’ orientation. The model appearances of Jupiter and Europa are generated with the Jupiter Viewer online tool from SETI (<https://pds-rings.seti.org/tools/>). While the shadow is captured by STIS in both exposures, the moon falls inside the aperture box only in the 2018 observation (odr212010) due to a larger phase angle on the 2019 occasion. This phase angle difference has a significant impact on the shadow’s location with regards to Europa, the separation being close to one Jupiter radius in 2019 and only around two Europa diameters in 2018.

To conclude, the STIS instrument provides spectrally and spatially resolved images, that also records in TIME-TAG, enabling temporal views of the shadow’s transit throughout

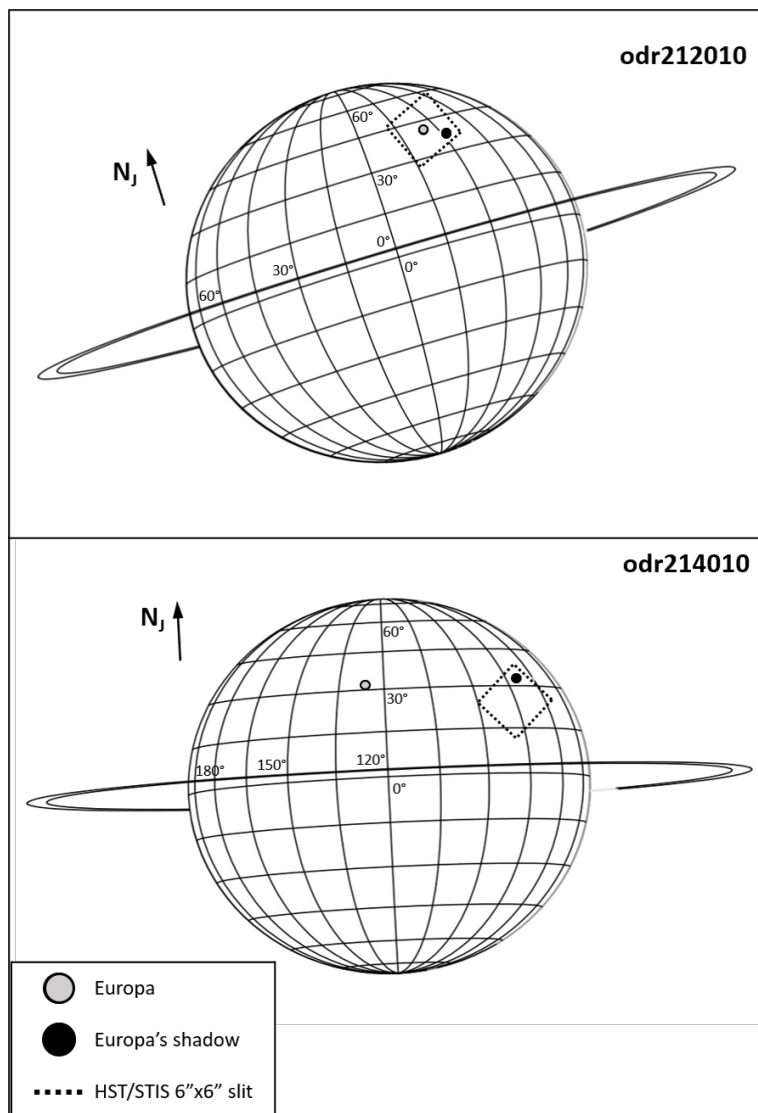


**Figure 3.3:** *Approximate viewing geometries of the observations, as seen from Earth and HST (generated with the Jupiter Viewer online tool from SETI), including the STIS aperture’s FOV. The top panel shows the 2018 observation and the bottom panel the 2019 observation. The coordinates are in system-III, and the Jupiter north vector  $N_J$  is also displayed. The vertical image direction is coincident with celestial north.*

an exposure. The G140L grating produces 2D-images in Ly- $\alpha$  that are available for analysis through partly calibrated *flt*-files, that also contain arrays with statistical errors and pixel quality information.

## 3.2 Image Processing

The images from observations odr212010 (May 5, 2018) and odr214010 (May 14, 2019) are displayed in Figure 3.4. They both show the full, uncut exposures, of the  $1024 \times 1024$  pixel detector with detector counts  $C(x, y)$  as unit. The counts are bounded to intervals that better display the dominant Ly- $\alpha$  image, where odr212010 generally has lower count rates than odr214010. The aperture is shifted off the 512 centre pixel on the  $y$ -axis

(cross dispersion) with approximately  $3''$ , to avoid areas with high dark current (Riley et al., 2019).

The available images from the *flt*-files require further processing before they can be analysed. The recorded detector counts need to be converted to physical units, so that the analysis can be related to physical quantities. Knowledge of the viewing geometry and the position of Europa's shadow is also important, for when performing the forward modelling.

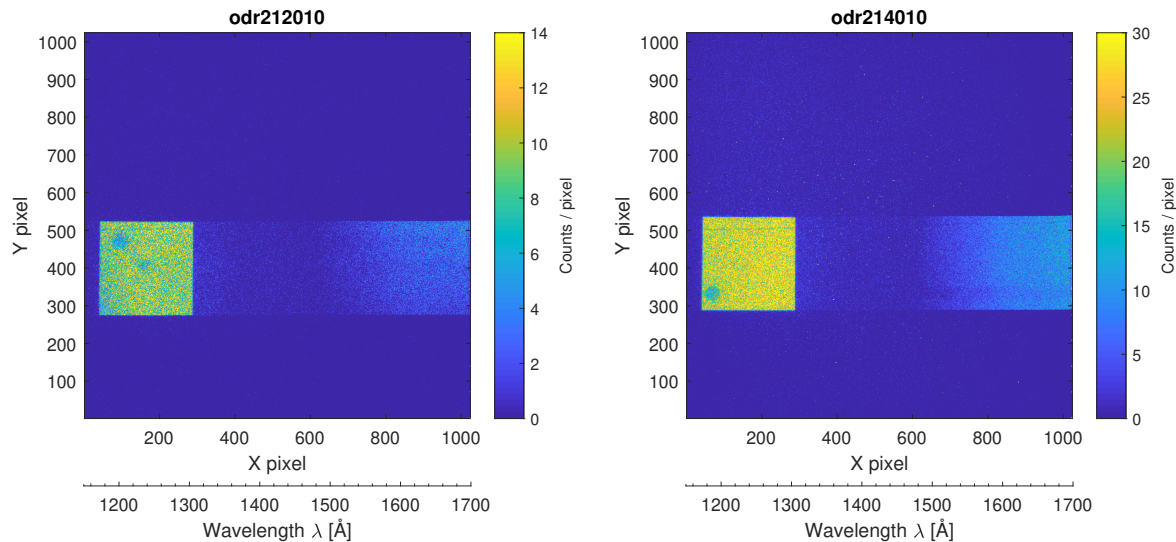


**Figure 3.4:** Full exposures of the 2018 (left panel) and 2019 (right panel) observations, in detector counts. The Ly- $\alpha$  aperture box is clearly visible towards the left detector side, while other wavelengths along the dispersion axis are less prominent.

### 3.2.1 Unit Conversion

A photometric conversion from detector counts to Rayleigh is performed, to associate the obtained images to a physical quantity. The Rayleigh unit is often used in photometry studies of airglow emissions and is defined according to Hunten et al. (1956) as

$$1 \text{ [R]} = \frac{10^6}{4\pi} \left[ \frac{\text{photons}}{\text{cm}^2 \text{ s sr}} \right]. \quad (3.1)$$

Several physical characteristics of HST and STIS need to be accounted for to do a proper unit conversion of the recorded signal. The conversion from detector counts/pixel  $C(x, y)$  in the *flt*-files to pixel brightness  $B$  [R] is given as

$$B \text{ [R]} = \frac{4\pi}{10^6} \frac{C}{T_{\text{exp}} \cdot A_{\text{eff}}(\lambda) \cdot \Omega}, \quad (3.2)$$

where  $C$  [counts/pixel] is the detector counts,  $T_{\text{exp}}$  [s] is the exposure time,  $A_{\text{eff}}(\lambda)$  is the wavelength dependent effective area of the telescope mirror,  $\Omega$  [sr] is the solid angle

covered by each pixel, and the constant  $4\pi \cdot 10^{-6}$  comes from the definition of Rayleigh in equation 3.1.

The detector counts  $C$  and exposure time  $T_{\text{exp}}$  are available in the *flt*-file (in the science array and file header, respectively). The solid angle  $\Omega$  for each pixel is given by

$$\Omega \text{ [sr]} = m_x \cdot m_y \left( \frac{2\pi}{3600 \cdot 360} \right)^2, \quad (3.3)$$

where  $m_x$  and  $m_y$  are the pixel plate scales (the pixel FOV) in  $x$  and  $y$  directions, with unit [arcsec]. For the G140L grating,  $m_x = m_y = 0.0246''$ . The numerical term is due to conversion from arcsec<sup>2</sup> to steradian.

The effective area  $A_{\text{eff}}$  is defined as the product of the unobstructed HST mirror area  $A$ , and the wavelength dependent photometric throughput  $T(\lambda)$ , specific to the telescope instrument:

$$A_{\text{eff}}(\lambda) = A \cdot T(\lambda). \quad (3.4)$$

With the HST mirror diameter being  $\varnothing = 2.4$  m, the area is  $A = \pi(\varnothing/2)^2 = 45\,238.9342$  cm<sup>2</sup>. The photometric throughput  $T(\lambda)$  is dimensionless and specifies the fraction of incident light at a particular wavelength, that reaches the detector after passing through the telescope. It is obtained from calibration files that are referenced in the *flt* header. Throughput at Ly- $\alpha$  is not specified in the calibration files, instead it is computed through linear interpolation using the two closest available wavelengths.

With formulas 3.2–3.4, the conversion of the recorded signal from counts to brightness in Rayleigh is demonstrated. The observations can thus be put into a physical context and can be compared to other studies.

### 3.2.2 Image Orientation

The images are oriented in the HST/STIS coordinate frame, as such they are rotated relative to the celestial J2000 and Jupiter frames. To better understand how the STIS view changes throughout the exposures, the image orientations in these other frames are examined, specifically relative to Jupiter’s north axis.

The orientation scheme is presented in Figure 3.5, where all axes are projected on the STIS image (detector) plane. The STIS frame is a right-handed coordinate system, with its primary axis along the telescope roll axis, and its other two axes aligned with the detector’s  $x$ - and  $y$ -axis. The aperture is almost aligned with the detector axes, but deviates slightly, up to  $1.5^\circ$  in rotation (Sohn et al., 2019). All angles are defined positive in the counterclockwise direction. The angles *ORIENTAT* (between celestial north and the detector  $y$ -axis) and *PA\_APER* (between celestial north and the aperture  $y$ -axis) are specified in the *flt*-file header. The angle  $\phi_N$  is the projected angle between celestial north and Jupiter north, onto the image plane, as seen from HST. It is computed with

the SPICE software toolkit from NASA’s Navigation and Ancillary Information Facility (<https://naif.jpl.nasa.gov/naif/toolkit.html>).

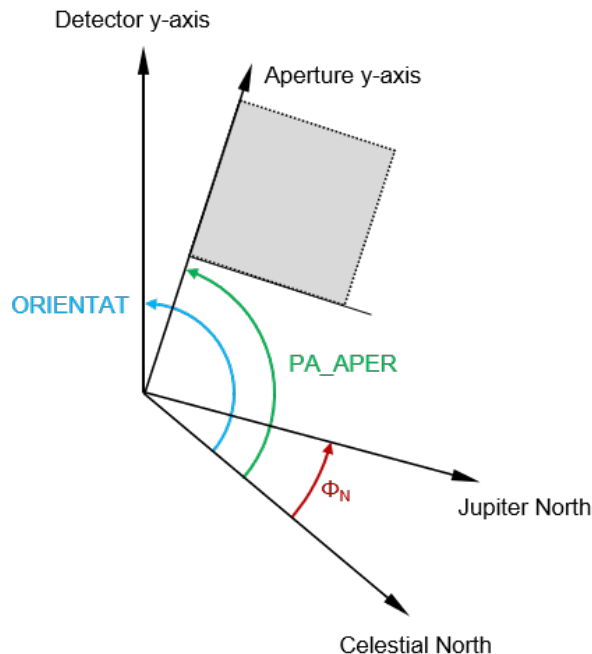


**Figure 3.5:** Illustration of the image orientation in STIS relative to celestial and Jupiter north. All vectors are projected onto the STIS image plane. The aperture box is visualized on the aperture  $y$ -axis.

The angle that orients the Jupiter north vector in the images is the difference between *ORIENTAT* and  $\phi_N$ , since the image analysis is based on the  $1024 \times 1024$  pixel array, in detector coordinates. This angle originates however at the Jupiter north vector. To get a more intuitive understanding of the orientation, the reversed angle is used, going from the detector  $y$ -axis to Jupiter north (with a counter clockwise angle still denoted as positive), which is defined as  $\theta_{\text{rot}}$  and is expressed as

$$\theta_{\text{rot}} = \phi_N - \text{ORIENTAT}. \quad (3.5)$$

For the two observations,  $\theta_{\text{rot}}$  is  $155.8^\circ$  and  $135.7^\circ$  for odr212010 and odr214010 respectively. The Jupiter north vector  $\mathbf{N}_J$  is displayed in the exposures in Figure 3.6. Observations and model images in this study are kept in their “original” orientation along the detector frame, and not rotated with Jupiter north pointing upwards, to better reference image locations in pixel pairs  $(x, y)$ .

### 3.2.3 Limitations on Exposure Time

During the observations, Europa and its shadow transit across Jupiter’s disk, while STIS is recording the incoming photon flux. In a final image, where the flux has been summed over time, it can thus be difficult to see if the objects have travelled outside of the jovian

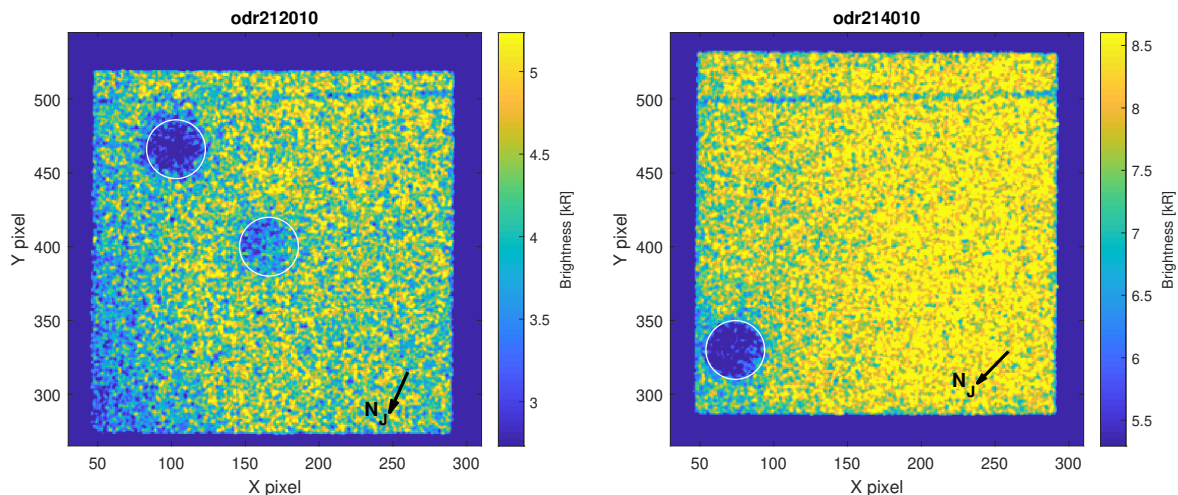


**Figure 3.6:** *The 2018 (left panel) and 2019 (right panel) observations in the Ly- $\alpha$  aperture box, with an applied filter for better visualization and with brightness in kR. The moon (in the aperture centre of odr212010) and shadow are encircled, and Jupiter north vectors are added. The MAMA repeller wire is also visible going horizontally over the detector at around  $y = 500$ .*

disk at any time. The TAG-TIME recording mode is therefore useful for reviewing the observation and to see what parts of the exposure that can be used.

Of the two observations, odr2102010 exhibits the shadow reaching the Jupiter limb in the latter half of its exposure. Figure 3.7 displays an accumulated (uncalibrated) image for the exposure’s last 200 seconds, showing the shadow’s proximity to the limb. The 2019 observation shows no limb coming into view, even though ephemeris tools (such as the Jupiter Viewer from SETI, and the SPICE toolkit from NAIF) suggest that the shadow goes off-limb after around 1 000 seconds. Instead there appears to be a flux increase inside the entire aperture box late in the exposure.

Since the resonant scattering contribution from the Ly- $\alpha$  line wings becomes more dominant close to the limb (Ben Jaffel et al., 2007; Clarke et al., 1991), limb emissions originate from a deeper H layer which possibly creates 3D-structures in the shadow. The image modelling in Section 3.3 assumes however that the shadow appears in a shallow H layer, much like a flat 2D shadow projection on a solid surface. This is valid within the limb as models from Ben Jaffel et al. (2007) indicate, but not at the limb.

To better accommodate for the assumption of a 2D-shadow, and to avoid observing it when having any other structure, the observations are thus cut to only include the time when the shadow is well within the limb, where the Ly- $\alpha$  line core dominates the scattering (Ben Jaffel et al., 2007; Clarke et al., 1991). For odr212010 this means that the time used for image modelling and analysis is 0–600 seconds. In this part of the exposure the limb is just outside the aperture FOV by the lower left corner of the detector image (around pixels  $(x, y) = (50, 290)$ ), which, with the aperture orientation in mind, allows for the assumption that the limb is at an adequate distance from the shadow.

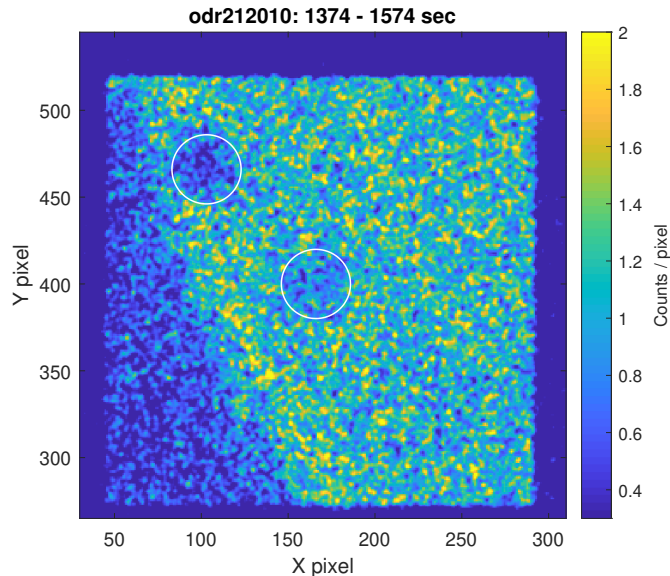


**Figure 3.7:** *The last 200 seconds of the odr212010 exposure, showing the Jovian limb in close proximity to Europa and its shadow.*

For odr214010 the whole exposure time is used, despite ephemeris models arguing for the shadow going off-limb. Since there is no visible limb, which should emerge first in the aperture’s upper left corner (around pixels  $(x, y) = (50, 520)$ ), the assumption of a flat shadow is still made. The cut exposures that are used for image modelling are displayed in Figure 3.8.

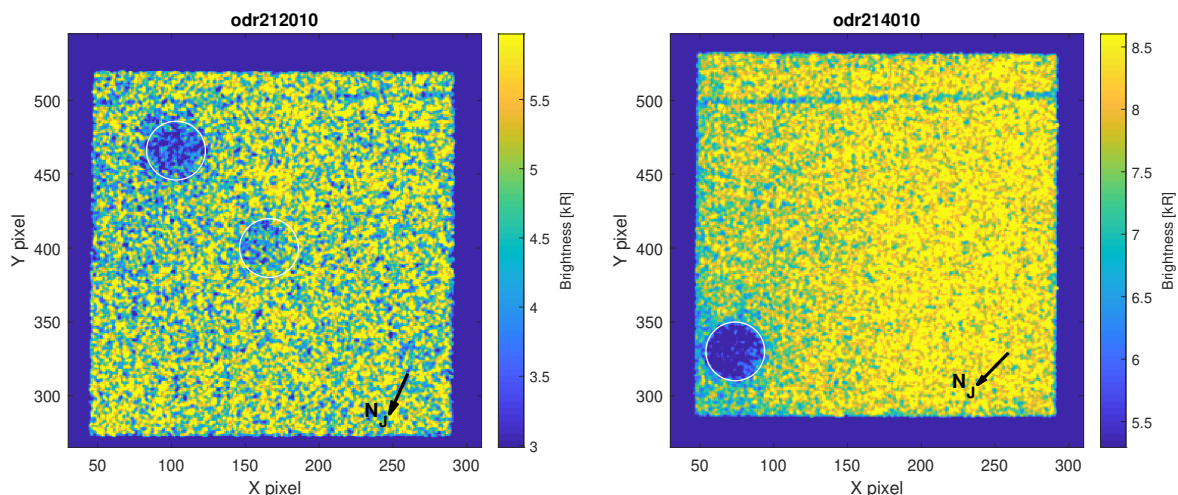


**Figure 3.8:** *Cut exposures of the observations, that are used for the image modelling and analysis. The first 600 seconds of odr212010 (left panel) are used, while the entire exposure time is used for odr214010 (right panel).*

### 3.2.4 Shadow Location

The image pixel resolution is around 80 km/pixel (see Table 3.1 for exact resolutions), meaning that a potential plume is likely only located 1–3 pixels above the shadow

limb. Having a correct location of the shadow is thus crucial for model images that are later compared to the observations, as a shift between model and observation by a few pixels can create false plume detections. A method for locating the shadow centre is thus presented here. The method does not however include locating Europa's disk in odr212010, since a detailed analysis of the moon is outside of the study's scope. Europa's location is instead estimated by eye.

The locating method is used in Giono et al. (2020). It investigates how the difference between model and observation varies around the shadow limb, along an angular profile. The objective is to find the pixel location that serves best as the model's shadow centre, which gives the smallest difference. (The creation of model images used here is presented in Section 3.3). For this the metric  $\epsilon$  is introduced, which is the standard deviation of the angular profile. To create the angular profile, the shadow limb region of the model and observation difference is first divided into angular bins. The profile is then created by taking the mean of the pixel values in each bin.

The limb bins span  $20^\circ$  azimuthally and  $0.3 R_E$  radially (or 5.97 pixels). Here, the bins are placed on the inside of the limb, as shown in Figure 3.9, instead of on the outside as in Giono et al. (2020), due to placement constraints created by the shadow's proximity to the aperture box edge in odr214010. This should not affect the method since model misplacement still generates bleed-through in the bins from the bright background.

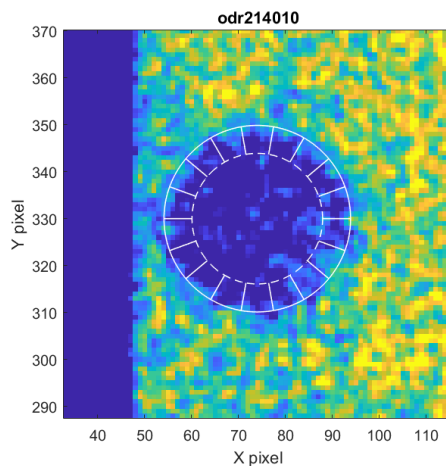


**Figure 3.9:** *Angular bins for locating the shadow centre, here illustrated for odr214010. The solid circle denotes the shadow limb, and the dashed circle is the radial limit of the bins.*

An important thing to consider regarding shadow location is its geometry. A large separation between moon and shadow would suggest a more elliptic shape, which is further elongated with a larger sunlight incidence angle. Due to the small phase angle in both observations however, the shape is assumed circular.

The locating method investigates an area in proximity to a starting guess and generates an array with  $\epsilon$ . The lowest value then indicates an angular profile with the smallest variance, and thus a best fit between model and observation. From the starting guess,

the model shadow is shifted  $[-4, +4]$  pixels in  $x$  and  $y$ . The limb bins are fixed in the model shadow frame, so they are shifted along with the model. This ensures that the model is always centred and that bleed-through only occurs due to model and observation misalignment. The model used for locating the shadow consists of a fitted background with shadow, and an applied point spread function (PSF), as further presented in Section 3.3.

For each pixel shift, the difference between model and observation is averaged in each bin, producing the bin profile. The standard deviation is then computed from this averaged profile, generating  $\epsilon$ . Figure 3.10 displays an epsilon array yielded from locating the shadow in odr214010, where the starting guess is  $(x, y) = (73, 331)$ . The best fit is shown to be with the shadow centre in  $(x_{sc}, y_{sc}) = (74, 330)$ . Applying the method on odr212010 yields the shadow centre in  $(x_{sc}, y_{sc}) = (103, 466)$ .

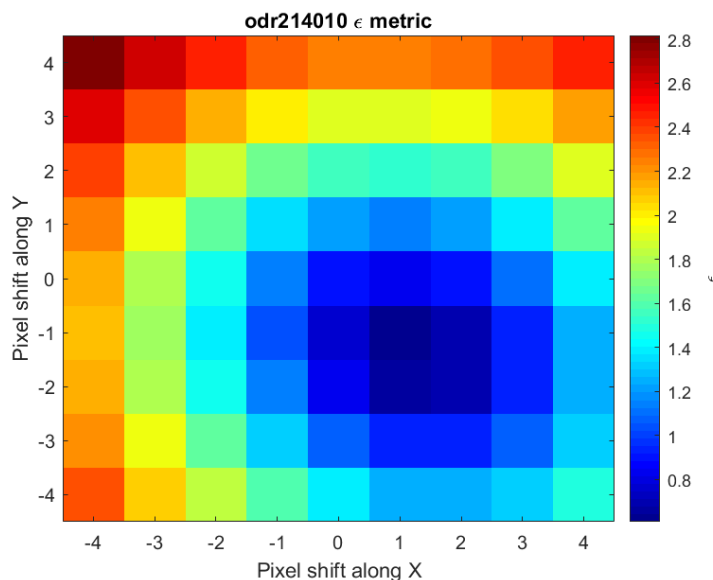


**Figure 3.10:** Resulting  $\epsilon$  array for odr214010, displaying the shadow location best fit as a  $(+1, -1)$  pixel shift from the starting guess  $(x, y) = (73, 331)$ .

The validity of the method is evaluated to ensure that the shadow centre is correctly located. Giono et al. (2020) mention that the observation needs adequate contrast between moon and background, which translates to shadow and background here. Furthermore, there cannot be too many off-limb features (e.g. plumes) that have a significant impact on the observation.

To validate the method, it was tested with artificial observations that were created by adding random Poisson noise to the model. This way the shadow centre is known beforehand. Multiple trials were then performed, where the model was shifted  $[-1, +1]$  pixels in  $x$  and  $y$ , to evaluate how often the centre is correctly determined relative to shifts of 1 and  $\sqrt{2}$  pixels. A new artificial observation was created for each trial.

From 1000 trials for the odr214010 observation, the shadow centre was correctly determined 71% of the time compared to a 1-pixel shift, and 96% of the time compared

to a  $\sqrt{2}$ -pixel shift, which is similar to Giono et al. (2020)<sup>1</sup> and is considered as satisfactory, giving confidence in the method’s validity. Performing the same validity test for odr212010 gave poor results however, due to prominent noise and low contrast when the exposure time is only 600 seconds. For this case, the rate of correct determination was too low to give any confidence in the obtained shadow location.

To obtain adequate contrast between shadow and background, the full odr212010 exposure was also investigated, to perform the trials and to determine the shadow location. It is assumed that this can be done for the described purpose, since the phase angle is so small that any 3D-structures ought not to show close to the limb, and the shadow location is only to be compared with the previous result. With 1000 trials for the full exposure, the rate of correct determination was 89% and 99%, compared to pixel shifts of 1 and  $\sqrt{2}$  respectively, giving confidence in the method for this exposure time. The centre was then determined to  $(x_{sc}, y_{sc}) = (103, 466)$ . This is the same location as for the shorter exposure time and is thus determined as the shadow centre.

### 3.3 Image Modelling & Analysis

This section deals with the forward modelling process, where artificial images are created. After considering possible Ly- $\alpha$  sources that contribute to the signal, models may be generated and compared with the observations, to investigate any anomalies that may be present at the shadow limb.

The image modelling process consists of three primary steps where no H corona at Europa is assumed. First, the Jovian background is reproduced with a polynomial surface fit. The shadow is then added by inspecting its observed value. Instrumental effects are applied last, consisting of a PSF that is characteristic of STIS, and the aperture box. The steps are illustrated in Figure 3.11.

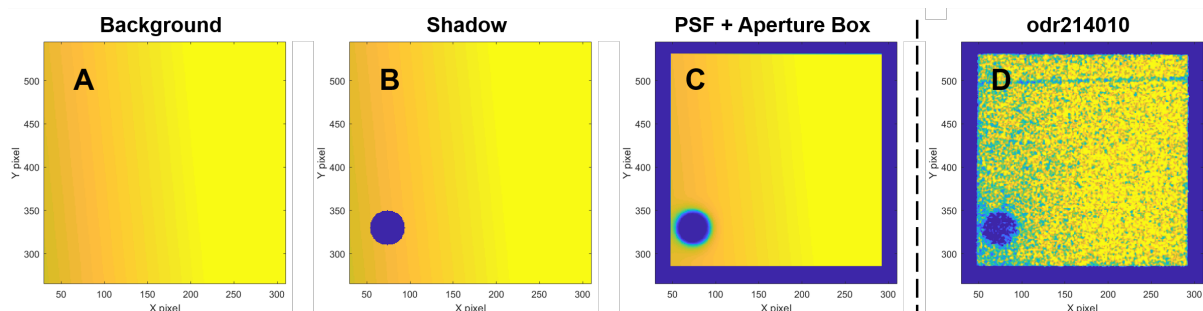


**Figure 3.11:** *The three primary modelling steps, here for odr214010. The background is first created (A), the shadow is then added (B), and lastly a point spread function and the aperture box are applied (C). Panel D shows the observation for reference.*

From the primary steps, the model is then expanded to include a corona, with a corresponding surface density  $n_{H,0}$  that agrees with the observation. The end result is

<sup>1</sup>The Giono et al. percentages were 83% and 97% for 1-and  $\sqrt{2}$ -pixel shifts, respectively, for 10000 trials.

a model that provides a best fit to the observation. However, performing the modelling according to the steps previously described, and evaluating best fits in consecutive order, does not necessarily yield the best result.

A best fit model needs to be provided by the collective contributions of the background surface, the shadow, and corona. An optimisation is therefore performed, where these variable parts are jointly evaluated for an overall best fit.

The optimisation is iteratively executed with the background surface already given. A simplex search method of Lagarias et al. (1998) is used, where the shadow's minimum value and the H surface density are the optimisation variables. In each iteration the polynomial order of  $x$  and/or  $y$  in the surface fit changes.

After a best fit is obtained, an image analysis is performed, where the shadow limb is investigated for localised signal extinctions, attributable to enhancements in water vapour. The individual modelling steps and the limb analysis are further explained in the subsequent sections.

### 3.3.1 Ly- $\alpha$ Contributions

Since it is the H Ly- $\alpha$  line that is analysed in this study, sources of H that may contribute to the signal in the images must be considered. Four main sources are considered here; the Jovian H dayglow that serves as the image background, the foreground emissions from the IPM and Earth's geocorona (considered as a combined source), the reduced Jovian emissions at Europa's shadow disk, and the reduced Jovian emissions due to the presence of Europa's H corona. A sketch of these contributions is shown in Figure 3.12.

The attenuation of solar radiation by Europa and its H corona are together considered to create the shadow on Jupiter. Hence, these are two separate sources from the moon that are modelled.

The combined foreground source of geocoronal and IPM H fills the aperture box. Their specific properties within the aperture's FOV are not considered in any way, they are only assumed to give a uniform Ly- $\alpha$  contribution over the entire image.

Jupiter covers the entire background in the images, thus there is no Ly- $\alpha$  source behind the plane of the shadow, and the foreground is the only contributing source other than the Jupiter dayglow. In odr212010 there is an extra subtraction of the Jupiter signal, occurring when the dayglow emissions pass through the corona at Europa once more, on the way to HST. This decrease must be accounted for in the model.

There may also be Ly- $\alpha$  absorption in Europa's atmosphere from other sources, generated through other processes such as excitation or electron-impact dissociation, and by other species such as H<sub>2</sub>, O<sub>2</sub>, OH and H<sub>2</sub>O. These sources are discarded however (though not for local H<sub>2</sub>O concentrations), due to negligible impact on the overall signal, as motivated by Roth et al. (2017).

There may exist Jupiter emissions when no solar resonant scattering occurs, such as in the

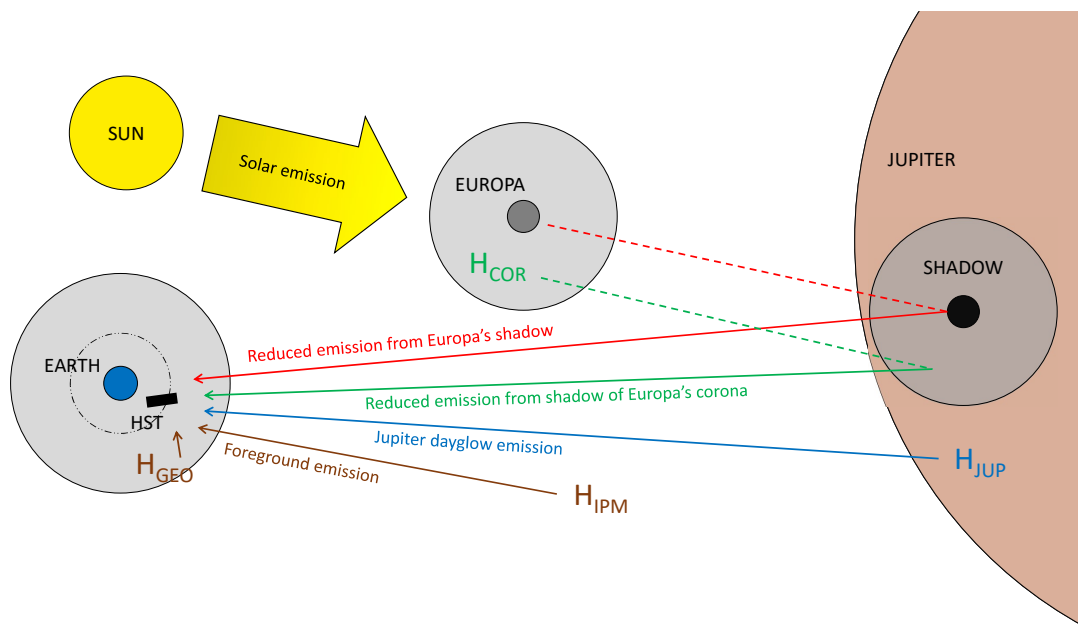


**Figure 3.12:** A not to scale illustration of  $H$  Ly- $\alpha$  sources that may contribute to the observed signal of HST. Solar emission is blocked by Europa, creating a shadow of reduced Jupiter emission (red), and is also scattered in Europa's  $H$  corona which is reflected around the shadow limb (green). The Jupiter dayglow makes up the entire background in the images (blue). Solar Ly- $\alpha$  is also scattered in the foreground by  $H$  the IPM and in Earth's geocorona (brown).

European shadow. This is presented in a Ly- $\alpha$  nightside map by Melin et al. (2016), which shows non-zero emissions on the hemisphere facing away from the Sun. An addition of Ly- $\alpha$  that would be visible in the shadow, would however also be present in the rest of the Jupiter dayglow. Furthermore, the underlying airglow emissions in the HST observations are reasonably lower than in the Melin et al. nightside map (which is in the order of 1 kR), due to the difference in solar cycle phase. Being lower than the shadow's general brightness in both exposures, it would be motivated to neglect such a small contribution. If present it would nonetheless be embedded in the shadow minimum brightness, and assumed constant in the aperture's FOV.

### 3.3.2 Creating Artificial Images

In the optimisation, a best fit is obtained by using the reduced chi-squared statistic,  $\chi_\nu^2$ . It computes how well a model compares to an observation, by evaluating if the model is in accordance with the error variance. A value close to 1 corresponds to a good fit.  $\chi_\nu^2$  is defined as  $\chi^2$  per degree of freedom,  $\nu$ :

$$\chi_\nu^2 = \frac{\chi^2}{\nu}. \quad (3.6)$$

The degree of freedom is computed as  $\nu = m - 1$ , where  $m$  is the sample size (i.e. number

of pixels used).  $\chi^2$  is the weighted sum of squared deviations and is defined as

$$\chi^2 = \sum_i^m \frac{(O_i - M_i)^2}{\sigma_{0,i}^2}, \quad (3.7)$$

where  $O_i$  is the observation value,  $M_i$  is the model value, and  $\sigma_{0,i}^2$  is the variance, all in pixel  $i$ .

A best fit is considered as the model that primarily gives the best  $\chi^2$  for radial brightness profiles of the shadow. This is because it is the area around the shadow that requires the best agreement with observations, to minimise the risk of identifying limb anomalies that exist only due to poor modelling. The  $\chi^2$  of the entire image (within the aperture box) is used as an additional measure of goodness-of-fit.

Observation and model radial profiles are generated by averaging the brightness values of all pixels in concentric rings, that are centred around the shadow. Figure 3.13 illustrates the profile's general shape. The rings are  $0.1 R_E$  wide (around 156 km) and extend radially outward from the shadow centre to  $5 R_E$ . In Roth et al. (2017) radial profiles were generated up to  $4 R_E$ , with  $0.05 R_E$  wide bins. Wider bins are used here to guarantee that at least one detector pixel is included radially ( $0.1 R_E$  is around two pixels). The extra Europa radius is added arbitrarily to include more of the model image.

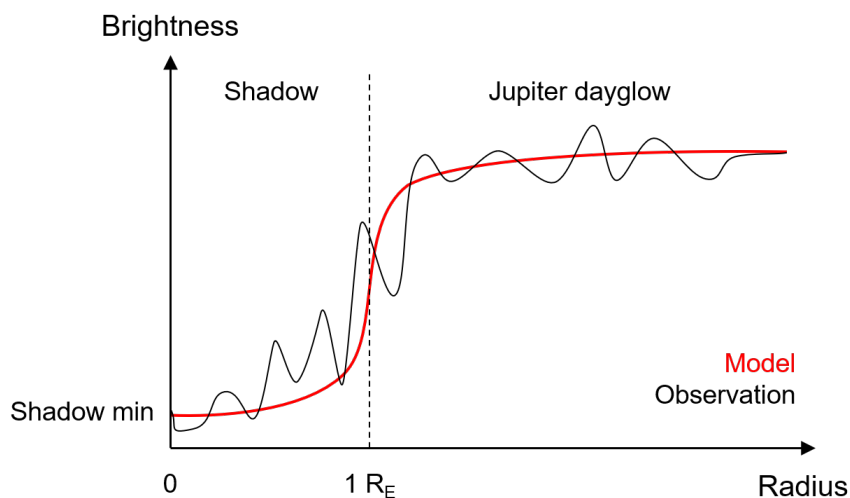


**Figure 3.13:** Illustration of model and observation radial profiles. The model (red) is fitted to the observation (black). The shadow, within  $1 R_E$ , generates a dip in the brightness, where the transition to the background is smoothed by the instrument PSF.

### Modelling Jupiter's Background

Jupiter's dayglow that serves as the images' background is modelled with a two-dimensional surface fit within the Ly- $\alpha$  aperture box. The area used for the fit is cut off approximately 5–10 pixels within the box edges, to exclude any edge effects created by the depiction of the aperture on the detector. The surface has different order polynomial

functions in  $x$  and  $y$ , these are decided during the model optimisation. Figure 3.14 displays example surface fits for odr214010 that are tested in the optimisation. Only polynomial orders of 1–3 in  $x$  and  $y$  are tested, to constrain what assumptions are made of the dayglow’s variability in the aperture box.

Regions containing Europa, its shadow and the repeller wire, are excluded from the surface fit, to avoid using pixels that are influenced by anything other than the dayglow. An exclusion radius of  $1.7 R_E$  at the shadow and moon is arbitrarily selected to avoid including a potential H corona (excluded regions in the background fit were arbitrary also in Roth et al. (2017) and Alday et al. (2017)). The excluded areas for odr214010 are visible in Figure 3.14, while the the excluded areas for odr212010 are displayed in Appendix C.

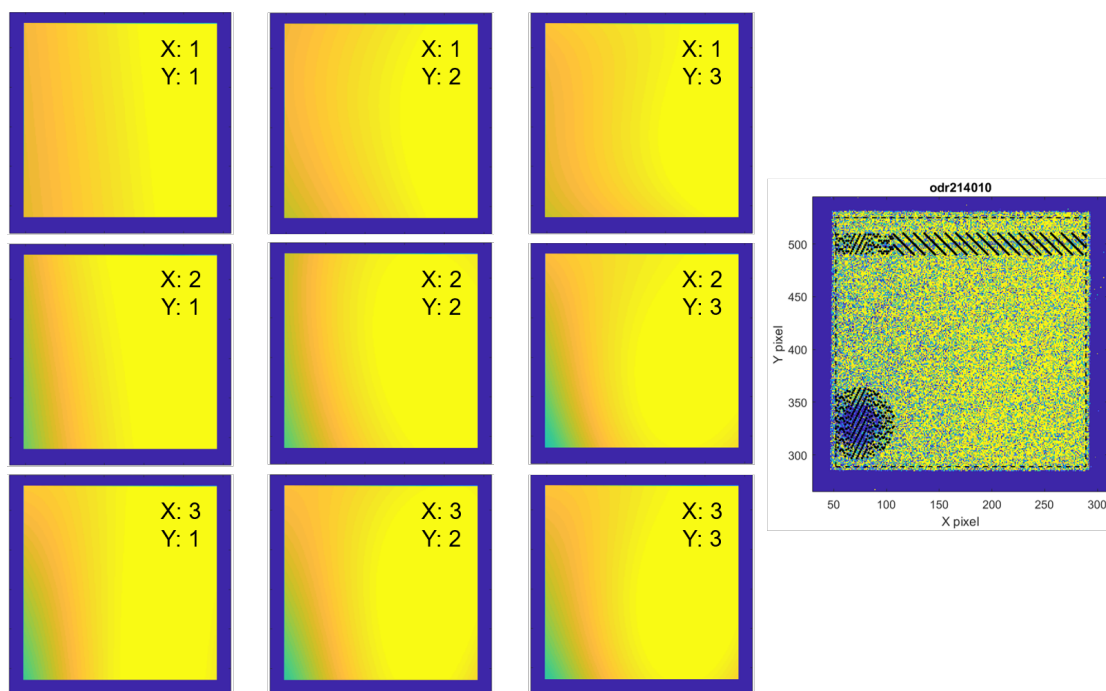


**Figure 3.14:** Example background surface fits for different order polynomials in  $x$  and  $y$ , for odr214010. Only polynomial orders of 1–3 are considered in the model optimisation (displayed in each panel). The areas excluded for the fit are visible in the far right panel (black dots).

### Modelling Europa’s Shadow

A model of Europa’s shadow is created in the model optimisation function. A first guess of the brightness in the shadow region is provided to initiate the optimisation. It is generated by computing the average brightness in the area within  $0.5 R_E$  of the shadow.

An underlying assumption is that Europa’s shadow is a circular disk with uniform brightness. The disk’s homogeneity is due to the assumption that the Ly- $\alpha$  contribution from the foreground is uniform.

As the Sun is an extended light source, the shadow may be influenced by a penumbra<sup>2</sup>, i.e. a blurring of the shadow border. Although the Sun is over 1 000 times further away from Jupiter than Europa, and a shadow with a completely sharp border may be an adequate approximation, the size difference between light source and object makes the presence of a penumbra not improbable. The transit image in Figure 3.2, displaying multiple Galilean satellites and their shadows, shows a visible penumbra in Callisto’s shadow, while such a feature in Europa’s shadow is less apparent.

A penumbra should be visible in all wavelengths if present, thus it is modelled in addition to the standard sharp-edged disk, during the primary modelling process. They can then be compared in the radial profiles to inspect if a penumbra is visible. A penumbra is modelled as a linear increase of the underlying background brightness, extending radially from the interior umbra border (at the shadow minimum brightness), to the penumbra border (see Appendix A for detailed calculations).

Special penumbra effects that alter the signals of water plumes and corona are disregarded. While these effects may be present, modelling them and taking their governing optical geometries into account are considered outside the scope of this study.

### Instrument Effects

To account for instrument effects generated when the photons travel through HST and STIS, a PSF and the aperture box are applied. The PSF is generated by the Tiny Tim software from Krist et al. (2011) and is convolved with the model to emulate the image smoothing that is produced by the instrument.

After the PSF is applied, the aperture box is added, so that it is only the Ly- $\alpha$  image that has non-zero brightness. The aperture tilt, that is represented by the difference between the angles *ORIENTAT* and *PA\_APER* (see Section 3.2), is also accounted for.

### Accounting for Europa’s Hydrogen Corona

Modelling a hydrogen corona is done by considering a density distribution of H on Europa. A radially symmetric corona is applied by e.g. Roth et al. (2017) and Alday et al. (2017), that is generated due to an assumed constant H temperature of 1 000 K (from simulation results of Smyth et al. (2006)), resulting in a fast escaping corona. The same corona is used here, therefore a profile for the H atom number density is assumed as

$$n_{\text{H}}(r) = n_{\text{H},0} \left( \frac{R_{\text{E}}}{r} \right)^2, \quad r \geq R_{\text{E}}, \quad (3.8)$$

where  $n_{\text{H},0}$  is the surface number density ( $r = R_{\text{E}}$ ),  $R_{\text{E}}$  is Europa’s radius and  $r$  is the radial distance.

---

<sup>2</sup>The penumbra is the outer shadow region where an extended light source is only partly obscured by an obscuring object. The region within the penumbra, the umbra, is fully obscured.

The density profile is used to integrate the line of sight (LOS) column density,  $N$  (Alday (2017) performs detailed calculations of this), which is a measure of the amount of attenuating matter that is visible along the slant path through the corona. For the shadow,  $N$  is only apparent off-disk, i.e. outside  $1 R_E$  (otherwise also present on-disk when observing the moon) and is described as

$$N(r) = n_{H,0} \frac{R_E^2}{r} \pi, \quad r \geq R_E, \quad (3.9)$$

with the same notation as in equation 3.8. The column density profile decreases with radial distance ( $\propto r^{-1}$ ) and is thus highest at the limb, where the associated signal decrease is also largest.

To integrate a corona in the image modelling, the transmittance  $T$  is used, which measures the ratio of transmitted and incident light intensity, according to the Beer-Lambert law as

$$T_s = \frac{I_t}{I_0} = e^{-\tau_s}, \quad (3.10)$$

where  $I_t$  is the transmitted intensity and  $I_0$  is incident intensity. The optical thickness  $\tau_s$  in the exponential term is the product of the column density,  $N_s$ , and the absorption cross section,  $\sigma_s$ , of an atmospheric species  $s$ , as  $\tau_s = N_s \sigma_s$ . This product relates equation 3.10 to equation 3.9 and enables an observed signal extinction to be converted to column density and ultimately surface density of an atmospheric species, like hydrogen. The optimisation uses  $N(r)$  in this way, to generate a corona that gives the best fit in  $T_H$  in the radial profile.

The H absorption cross section changes for different Ly- $\alpha$  emission spectra. For the assumed atom temperature of 1 000 K, Roth et al. (2017) determines a cross section for resonant scattering H as  $1.9 \times 10^{-13} \text{ cm}^2$ . This cross section is used here, but only for when the corona scatters light from Jupiter's dayglow, i.e. at Europa in odr212010.

For the corona's shadow, the absorbed light originates instead in the solar Ly- $\alpha$  line, a much wider spectral profile with more energy than Jupiter's dayglow. This means that the coronal H absorption cross section for solar emissions is instead  $\sigma_{H,SUN} \approx 2.9 \times 10^{-15} \text{ cm}^2$  (a result from a radiative transfer analysis in Alday (2017)), which is two orders of magnitude smaller than for the absorption of the Jupiter background emissions (modelled in Roth et al. (2017)).

### 3.3.3 Shadow Limb Analysis

An image analysis is performed after the modelling, where the generated model is compared with the observation. This is done to evaluate if any signal extinction is present around the shadow limb, that may be attributed to an enhancement of water vapour (and a plume). Any such anomaly would be manifested as a very local decrease in brightness,

on the order of a few pixels in size (Roth et al., 2014; Sparks et al., 2016).

Water vapour at the European limb, reproduced in the shadow, can be detected by using the transmittance of water vapour,  $T_{\text{H}_2\text{O}}$ , in equation 3.10 for a given signal. The transmittance is estimated as the brightness difference between the model and observation, which is computed by first subtracting the minimum shadow value from observation and model, and then dividing the observation residual with the model residual.

Equation 3.10 is then solved for  $\tau_{\text{H}_2\text{O}}$ , from which  $N_{\text{H}_2\text{O}}$  can be retrieved. The column density provides an estimate of the water vapours magnitude, which is compared to previously derived column densities (e.g. Roth et al., 2014). The  $\text{H}_2\text{O}$  absorption cross section at Ly- $\alpha$ , as used by Roth et al. (2017), is  $\sigma_{\text{H}_2\text{O}} = 1.5 \times 10^{-17} \text{ cm}^2$  and is roughly constant near the Ly- $\alpha$  wavelength, and therefore independent of the line shape of the probed signal (Yoshino et al., 1996).

To minimise the assumptions made when analysing the shadow, no H corona is added beforehand. An angular profile is generated that azimuthally goes around the shadow limb in angular bins, to investigate anomalies. It is produced by taking the mean value of all pixels within each bin, as done in the radial profile.

The bins are  $15^\circ$  wide azimuthally (24 bins in total), that extend  $0.16 R_E$  radially ( $\sim 3.18$  pixels), with the zero-degree position at  $1 R_E$  in the detector  $x$ -direction from the shadow centre,  $(x_{sc} + 1 R_E, y_{sc})$ . Figure 3.15 shows the shadow in the two observations, with the angular bins.

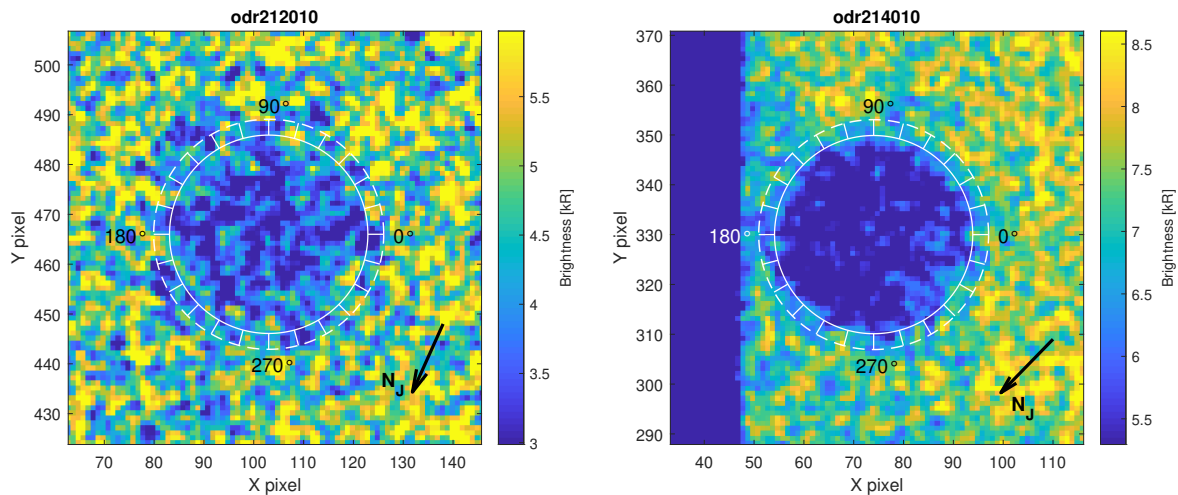


**Figure 3.15:** Angular bins for analysing the region above the shadow limb. The solid circle denotes the limb, and the dashed circle is the radial limit of the bins. Left panel: odr212010. Right panel: odr214010.

# Chapter 4

## Results

This chapter presents results that are obtained from the modelling and image analysis. The fitted model images are first presented, thereafter the resulting radial and angular profiles are discussed, where the angular profiles are evaluated with respect to their statistical properties.

### 4.1 Model Results

The best fit model images are displayed in Figure 4.1. A penumbra yielded the best agreement with the observation in odr212010, while a best fit for odr214010 was provided without a penumbra. The best background fit has a third order polynomial in  $x$  and a first order polynomial in  $y$  for odr212010. The best fit model for odr214010 has polynomial orders of two in  $x$  and three in  $y$ . Table 4.1 presents general properties of the generated models and image analysis.

**Table 4.1:** *Properties of the best fit models, displaying the shadow minimum, average Jupiter dayglow, H surface density, if a penumbra is included, chi-squared and upper limit water plume column density.*

Dataset	Shadow minimum [kR]	Avg. Jupiter dayglow [kR]	H surface density, $n_{\text{H},0}$ [ $\text{cm}^{-3}$ ]	Penumbra in best fit (Yes/No)	Best fit $\chi^2_{\nu}$ : Radial profile (entire image)	Upper limit $\text{H}_2\text{O}$ plume col. density [ $\text{cm}^{-2}$ ]
odr212010	3.39	5.10	0	Yes	1.15 (1.63)	—
odr214010	4.81	8.05	$1.36 \times 10^3$	No	1.14 (1.10)	$6.74 \times 10^{16}$

The radial profiles of the two observations and their fitted models are displayed in Figure 4.2. The profiles are primarily for inspecting the visibility of a hydrogen corona in the data, but also to examine the transition from shadow to background. There are dips in the otherwise smooth curves, present in both profiles at  $2.8 R_{\text{E}}$  and  $2.1 R_{\text{E}}$  for odr212010 and odr214010, respectively. These are due to asymmetrical cut-offs of the bins at the aperture edges in  $x$  and  $y$  directions (see Appendix B) and are present in the observations as well.

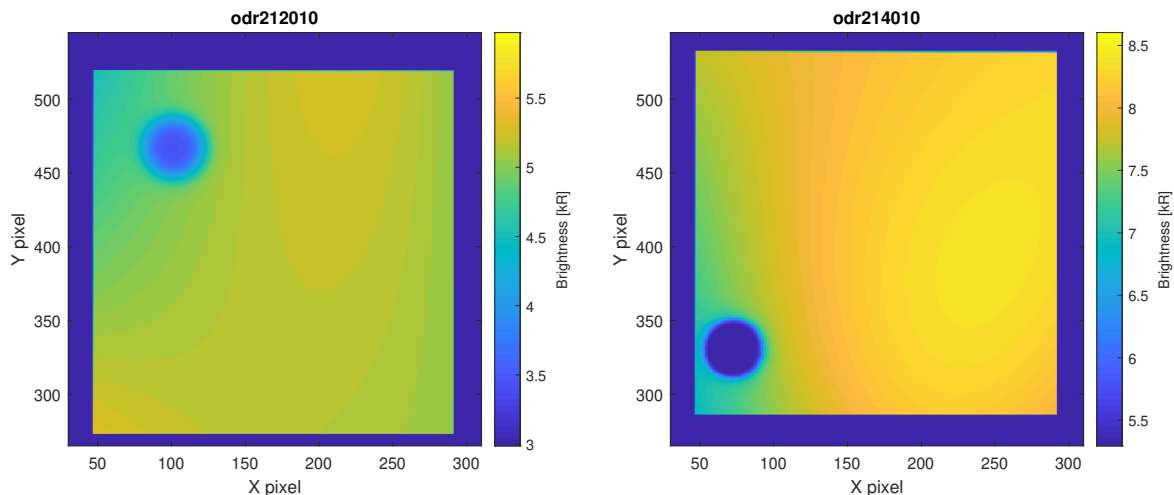


**Figure 4.1:** Resulting model images that provide the best fits to observations. The Jovian background is generally brighter in odr214010 (right panel) than in odr212010 (left panel). The background fits have polynomial orders of three ( $x$ ) and one ( $y$ ) in odr212010, and two ( $x$ ) and three ( $y$ ) in odr214010.

For the 2018 observation, a best fit to the profile is obtained without a corona present. An added penumbra also appears to provide a better fit (yielding a profile  $\chi^2_\nu = 1.15$ , rounded to the nearest two decimals) than a model without ( $\chi^2_\nu = 1.58$ ).

A model with surface density  $n_{\text{H},0} = 2 \times 10^3 \text{ cm}^{-3}$  as reported by Roth et al. (2017) is added to the profile for comparison, which consistently has  $\sim 100 \text{ R}$  lower brightness than the best fit outside of the shadow. The poor fit of this curve is due to bad modelling of the Jupiter background. When fitting a surface to the background, only a region out to  $1.7 \text{ R}_\text{E}$  is excluded at Europa (in addition to the shadow and repeller wire), while the H corona around the moon has an apparent influence on the brightness outside of this region. The corona is thus already taken into account in the modelled background, thus leading to a bias for zero H surface density further away from the shadow.

The best fit to the 2019 observation has a corona with surface density  $n_{\text{H},0} = 1.36 \times 10^3 \text{ cm}^{-3}$  (see the red dashed curve in the right panel of Figure 4.2), which gives a  $\chi^2_\nu = 1.14$ . The curve fits well to the observation, as does a model without a corona, which has a  $\chi^2_\nu \approx 1.14$  that is only larger in the third nearest decimal. An added penumbra does not however appear to fit well in this case, with  $\chi^2_\nu = 2.29$ . Why the penumbra only fits one of the two profiles is discussed in Chapter 5. A penumbra will nonetheless continue to be accounted for in the odr212010 model angular profile.

In total, the curves with best fits of surface density have data points that generally lie within the uncertainty of the observations, as do the null curves (it is for example the best fit of odr212010). The non-detection of a corona in odr212010 will remain as a result in Table 4.1, despite it being due to a bad background model, though this is further discussed in Chapter 5.

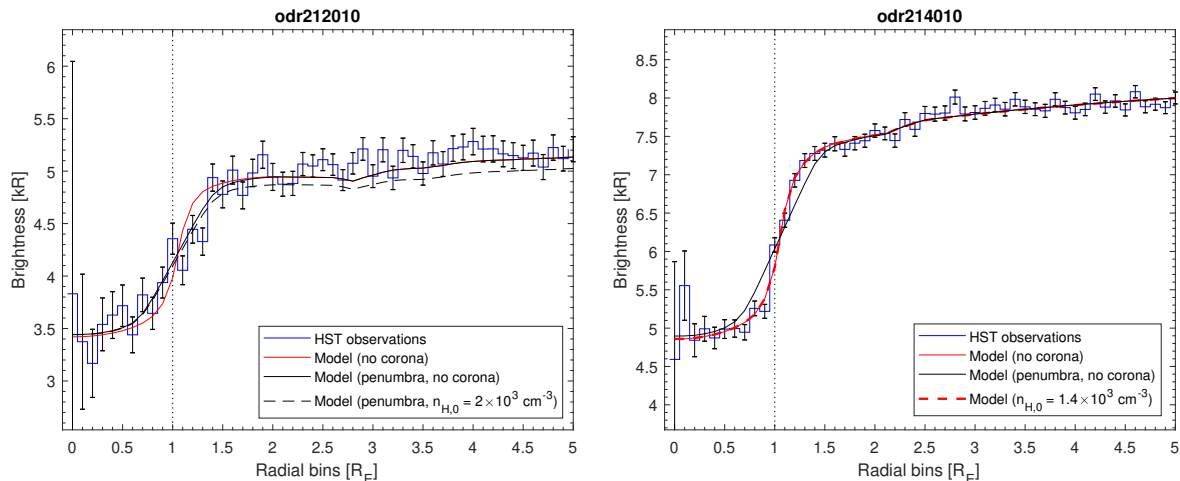


**Figure 4.2:** *Radial profiles of the observations and models. The dotted vertical line denotes Europa’s limb. The model with the best fit to odr212010 (left panel) is the black solid curve (with a penumbra and no corona). In odr214010 (right panel) the best fit is the red dashed curve, without a corona and with a  $1.4 \times 10^3 \text{ cm}^{-3}$  H surface density.*

## 4.2 Limb Analysis Results

The angular profiles that show the behaviour around the shadow limb are visible in Figure 4.3. They display how the model images are comparable to the observations, and how limb variations stand in relation to statistical uncertainty. A signal extinction corresponding to an  $\text{H}_2\text{O}$  LOS column density of  $1.5 \times 10^{16} \text{ cm}^{-2}$ , as detected by Roth et al. (2014b), is also added to one limb bin in each model, where a prominent dip in the observation’s profile is visible.

When comparing the observations with the models, two noteworthy outliers are visible, one in each observation. In the odr212010 profile there is a reduction of 1.23 kR relative to the model at  $\sim 350^\circ$ . In odr214010 it is located at  $\sim 280^\circ$  with a 0.96 kR reduction. Their bin locations (shaded in green in Figure 4.3) correspond to a southwest and northwest limb location, respectively. The two outliers correspond to  $\text{H}_2\text{O}$  column densities of  $3.07 \times 10^{17} \text{ cm}^{-2}$ , for odr212010, and  $4.72 \times 10^{16} \text{ cm}^{-2}$  for odr214010. These column densities are in the same orders of magnitude as those reported by Sparks et al. (2016) ( $\sim 10^{17} \text{ cm}^{-2}$ ) and Roth et al. (2014b) ( $1.5 \times 10^{16} \text{ cm}^{-2}$ ).

The transmittance estimation in Subsection 3.3.3, for deriving  $N_{\text{H}_2\text{O}}$ , subtracts the shadow minimum before the observation-model ratio. This way of computing the transmittance  $T$  requires the observation to be brighter than the best fit shadow minimum, to not get  $T < 0$ , which is mathematically incorrect for the logarithmic function in equation 3.10. This is however not the case for the odr212010, where the outlier at  $350^\circ$  is 178 R lower than the shadow minimum at 3.39 kR. To obtain a value for the column density, the transmittance is in this case set to 1% (99% signal attenuation), a placeholder for complete attenuation.

Examining the statistical properties, the measurement standard error,  $\sigma_0$ , in each bin

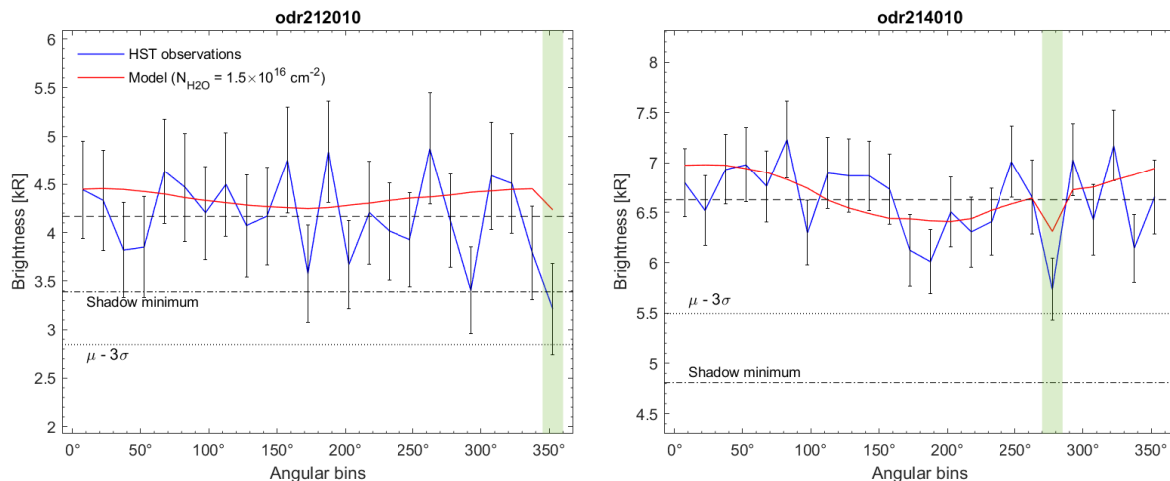


**Figure 4.3:** Angular profiles of the observation and model limb. No corona is modelled. The model of odr212010 (left panel) includes a penumbra, while there is no penumbra in the odr214010 model (right panel). The dashed line denotes the observation average value, the dash-dotted line denotes the shadow minimum value and the dotted line denotes the  $3\sigma$ -limit from the observation average. A signal decrease corresponding to a  $1.5 \times 10^{16} \text{ cm}^{-2}$   $\text{H}_2\text{O}$  column density is added to the model, in the bin that sees the largest signal extinction in the observation relative to the model (shaded in green).

is a first measure of an outlier’s significance. This error is assumed to only be the statistical fluctuation of the counts per detector pixel, while systematic errors like model imperfections and other instrumental errors are neglected. In the odr212010 profile the outlier is  $2.63\sigma_0$  from the model value, for odr214010 it is  $3.10\sigma_0$ . If a limit for significance is placed at  $3\sigma_0$  (which includes 99.73% of values in a gaussian distribution), only the outlier in the 2019 observation is significant.

A more conservative measure is to use the statistical mean  $\mu$  (interpreted as the expected value) and standard deviation  $\sigma$  of an observation’s profile. This measure assumes that the profile’s variability around the mean value is only due to noise. The value  $\sigma$  should also account for more sources of error than what  $\sigma_0$  does, since it is derived from the data. An outlier thus has to lie outside of  $3\sigma$  from  $\mu$  (visible as the dotted line in Figure 4.3) to be significant, which none of the outliers in the observations do ( $2.17\sigma$  for odr212010 and  $2.37\sigma$  for odr214010).

If the more conservative approach is used, there is no significant outlier in the observations that is indicative of  $\text{H}_2\text{O}$  attenuation. An upper limit on  $\text{H}_2\text{O}$  column density can however be determined, to confine the possible densities that are still consistent with the data. For this, only the 2019 angular profile is used, since the 2018 profile outlier already gives complete signal extinction. The upper limit is derived from the difference between the  $(\mu - 3\sigma)$ -line and the model, in the bin at  $280^\circ$  containing the outlier, which yields  $6.71 \times 10^{16} \text{ cm}^{-2}$ .

# Chapter 5

## Discussion

The method of studying Europa’s Ly- $\alpha$  shadow in search of water vapour enhancements around its limb is shown to provide results that are comparable with previous studies made of the moon. As only the shadow is examined here, a simplified model can be created that disregards parameters of the European surface that may influence limb detections, such as surface reflections and aurorae (Roth et al., 2017; Roth et al., 2016). The shadow’s proximity to the aperture box edges and the detector’s repeller wire influences the shadow location method and the radial bins. This does not necessarily affect the results however, as Europa’s disk is close to the aperture edges in other studies, while the results remain seemingly unaffected (e.g. Roth et al. (2017) that uses a  $52'' \times 2''$  slit). Future observations using a wide aperture should nonetheless try to keep the shadow centered, to minimise potential edge effects and to show more of the surrounding Jovian dayglow.

The resulting models fit well to the observations, where reduced chi-squared values of the entire images are 1.63 (odr212010) and 1.10 (odr214010). The models’ shadow minima include the foreground emissions from the IPM and geocorona, with values of 3.39 kR and 4.81 kR, which is comparable to observations of Europa by Roth et al. (2017) that had foreground emissions of 3.76–6.82 kR. The average Jupiter dayglow of 5.10 kR and 8.05 kR (see Table 4.1) also agrees with that of Roth et al. (5.24–9.34 kR).

### 5.1 Water Plumes

The associated H<sub>2</sub>O column densities of the angular profile outliers are in the same orders of magnitude as the detections in Roth et al. (2014b) and Sparks et al. (2016). However, as they lie between two and three standard deviations from the expected value, they cannot be claimed as detections, though it does not necessarily imply their non-existence. The derived upper limit column density of  $6.71 \times 10^{16} \text{ cm}^{-2}$  from odr214010 puts a constraint on the possible densities that may be detected. The detections from Sparks et al. (2016) of  $(0.7\text{--}3.3) \times 10^{17} \text{ cm}^{-2}$  can hence be excluded, but not the Roth et al. (2014b) detection of  $1.5 \times 10^{16} \text{ cm}^{-2}$ .

The statistical uncertainty is generally higher for odr212010 than for odr214010, in both the radial and angular profiles. This is probably due to the low exposure time of 600 seconds that generates low signal to noise and a low contrast between shadow and background. The low contrast is arguably also the cause for the small brightness difference between angular profile and shadow minimum (that includes the foreground emissions), which prevents a derivation of a column density upper limit for odr212010. odr214010 has, in addition to a generally brighter Jovian dayglow, a longer exposure time, indicating that at least one of these factors is necessary for a satisfactory analysis.

## 5.2 Jupiter Background

It is possible that the difference in background brightness on the two occasions is due to different solar fluxes, although similar flux values on the two dates in composite Ly- $\alpha$  time series from LASP (2020) do not support this idea. More likely, the difference is explained by different shadow locations, where the odr214010 location in system-III longitude coincides with the H bulge region according to the Melin et al. (2016) map. This produces a brighter dayglow than in odr212010, where the shadow is located outside the bulge.

The odr214010 shadow location may also explain the Jupiter limb disagreement between the observation and ephemeris tools. If an increased H abundance is present in the bulge, due to e.g. electron recombination by  $H_3^+$  as Melin et al. (2016) suggests, one may speculate that this can somehow generate a local protrusion in the corona, extending the limb in Ly- $\alpha$  far above the 1-bar pressure altitude (which defines the Jovian radius in the ephemeris tools according to Archinal et al. (2018)).

It could be further suggested that the brightness increase that occurs late in the exposure is due to Jupiter's rotation, bringing the bulge's peak intensity region into view. This would speak for the idea that it is Ly- $\alpha$  from the bulge that fills the aperture box. While the disagreement is an interesting phenomenon that can be investigated further, the image analysis should still primarily rely on what the observation shows and not on ephemeris tool results.

## 5.3 Shadow

Europa's shadow is assumed to be manifested as a 2D-silhouette on the top of Jupiter's Ly- $\alpha$  scattering corona. As the modelling process is based on this assumption, it needs to be valid. This is what models from Ben Jaffel et al. (2007) and Ly- $\alpha$  line profiles of Clarke et al. (1991) indicate, as they show that the scattering is dominated by the optically thick line core on most of Jupiter's disk. Coupled with the restriction that the shadow is only analysed when located well within the Jovian limb, the 2D-assumption is deemed as valid. A more thorough investigation of potential 3D-structures, than what is done here, should however be conducted before they are dismissed. They may create unknown effects that have significant impact on the observations.

### 5.3.1 Elliptic or Circular Shadow

Another assumption that largely governs the study's results is that the shadow is treated as an ideal circular disk and not as an ellipse. If it in reality is elliptic in shape, the shadow could bleed into the angular limb bins and create false signal extinctions. It is not clear however if such a bin brightness decrease is discernible from noise, and it would also depend on the elliptic eccentricity.

Furthermore, the phase angles of  $0.66^\circ$  and  $5.39^\circ$  on the two occasions are regarded as too small to create a noticeable ellipse. If the shape is nonetheless elliptic, it is reasonable to assume that its major axis would be oriented along to the moon-shadow line, which in both observations intersects the shadow limb at approximately  $315^\circ$  (using the notation of the angular limb bins). A shadow elongation in this direction is not apparent in either observation, and the circular approximation is therefore considered adequate. Still, the azimuthal variability of the shadow radius should be further examined, if a detailed analysis of the shape is wanted.

### 5.3.2 Shadow Penumbra

In the radial profiles, a penumbra is shown to provide a best fit to odr212010, but not to odr214010. It is difficult to understand why a penumbra is only present in the observation of weakest signal, as it should be present on both occasions (especially in odr214010 that has the stronger signal) and appear in a similar way to that of Callisto's shadow in Figure 3.2. One possibility is that the penumbra's influence is too weak in contrast to the bright background in odr214010, which also would mean that the penumbra model is faulty, since all contrast ranges should be covered by the model.

A more probable explanation is that the linear transition in odr212010 is not caused by a penumbra, but is solely due to noise. This seems likely since the shadow in the 600-second exposure has very variable brightness, with a mean value only  $\sim 1$  kR lower than the off-limb average (according to the angular profile). The high uncertainty in odr212010 is also more forgiving to a non-penumbra model, having a reduced chi-squared of 1.58, whereas the penumbra model in odr214010 yields a much higher value of 2.29. If a penumbra is absent it simplifies the assumptions about the observations, although it cannot be fully dismissed without investigating the optical geometry further.

## 5.4 Hydrogen Corona

Further examining the radial profiles of Europa, only the 2019 observation appears to exhibit an H corona, with a  $1.36 \times 10^3 \text{ cm}^{-3}$  surface density as a best fit, which largely agrees with previously reported  $n_{\text{H},0} \approx 2 \times 10^3 \text{ cm}^{-3}$  by Roth et al. (2017) and Smyth et al. (2006). However, the null curve (without a corona) is also well fitted to the observation and has a  $\chi^2_\nu \approx 1.14$ , that is only larger than the best fit in the third nearest decimal. Both curves lie close to the observation, hence a corona detection cannot be claimed nor excluded in this observation.

The 2018 observation exhibits instead a large difference between the best fit null curve and  $2 \times 10^3 \text{ cm}^{-3}$ . This is most likely due to bad modelling of the Jupiter background when Europa is close to its shadow, as described in Section 4.1. The H absorption cross section is higher for scattered Ly- $\alpha$  emitted from Jupiter than from the Sun (Alday, 2017), so the modelled corona around Europa has a much higher apparent attenuation than around its shadow, which extends far in the image and is not covered by the region at Europa that is excluded from the background surface fit. The corona is therefore unintentionally accounted for in the background model and thus leads to a bias for a zero H surface density.

The odr212010 signal is weak overall and a corona may also be masked somewhat by noise, regardless of good or bad modelling, however this is likely not enough to completely hide a detection. Though it is probable that the background model is bad, no remodelling is performed and the non-detection remains as the final result in this case. This problem should instead be considered in future observations, either by modelling the image in a different way when Europa is close to its shadow, or by avoiding these viewing geometries and opt for when the shadow is by itself, like in odr214010.

Considering that both observations show weak or no indications of a corona, it is concluded that it cannot be detected here. Since strong evidence for a  $2 \times 10^3 \text{ cm}^{-3}$  surface density corona nonetheless exists (Roth et al., 2017), it is justified to argue for the new method of observing Europa's shadow being well suited to use when searching for water vapour, without the signal being significantly influenced by coronal H. If the purpose is to detect a corona, it would be better to observe the moon itself. The method can potentially also be used for other icy moons when searching for atmospheric species with large  $\sigma_{\text{SUN}}$ .

# Chapter 6

## Conclusion

In this study Europa's Ly- $\alpha$  shadow on Jupiter is examined in search of reduced emissions that may be due to water plumes. This is a new method of performing this kind of research, as the moon itself is otherwise observed. Two observations that were made with the Space Telescope Imaging Spectrograph (STIS) on board the Hubble Space Telescope (HST) in 2018 and 2019 are used for the analysis.

Forward modelling is applied to create artificial images that are compared to the observations. Any anomalies around the shadow limb are then analysed and evaluated relative to their statistical significance. Assumptions that simplify the modelling process are made, like assuming an ideal circular 2D-shadow on Jupiter's H scattering corona. These assumptions are deemed valid, but detailed investigations may be needed to better understand their physical properties.

The modelled artificial images generally agree with the observations. Produced radial profiles of the shadow cannot confirm the existence of a hydrogen corona at Europa, as has been previously detected by Roth et al. (2017). This is due to a smaller H absorption cross section when spectrally wide solar Ly- $\alpha$  is scattered in the comparably cold corona and creates the shadow. The insensitivity of H is yet favorable for the search of water plumes at the limb, since the influence by coronal H is decreased.

Angular limb profiles are created that investigate shadow limb anomalies. Two noteworthy outliers are found at the limb (one on each occasion) corresponding to H<sub>2</sub>O line of sight column densities of  $3.07 \times 10^{17} \text{ cm}^{-2}$  and  $4.72 \times 10^{16} \text{ cm}^{-2}$ , for the 2018 and 2019 observation, respectively. They are however not statistically significant, with deviations from the expected value of  $2.17\sigma$  and  $2.37\sigma$  respectively, and can therefore not be claimed as detections.

A weak signal in the 2018 observation due to short exposure time and low contrast between shadow and background further prohibits any detection with a lower column density than what is derived. The weak signal is also the likely cause of a penumbra that appears to be present in the shadow on this occasion, and is ultimately attributed to noise. A penumbra should however be present in both observations, as this depends on

optical geometry and can generally be seen in the shadows of Galilean moons in visible wavelengths. A detailed analysis on the penumbra is required to better understand its physical properties in the Jovian Ly- $\alpha$  emissions.

With the 2018 observation having too weak of a signal, only the 2019 observation is used to compute an upper limit on H<sub>2</sub>O column density that confines the possible densities that are still consistent with the data. An upper limit of  $6.71 \times 10^{16} \text{ cm}^{-2}$  is derived, with which column densities of  $(0.7\text{--}3.3) \times 10^{17} \text{ cm}^{-2}$  as detected in 2014 by Sparks et al. (2016) can be excluded, while a  $1.5 \times 10^{16} \text{ cm}^{-2}$  column density as detected in 2012 by Roth et al. (2014b) cannot be excluded.

This new method of analysing Europa's far-ultraviolet shadow is conclusively regarded as a useful way of looking for potential plume signals, and may provide an additional aid in the search of extraterrestrial life. Although no detections of plumes are made, the results are comparable with previous studies that have only observed Europa itself. If plumes are present, the results in this study speak for the notion of irregular plume activity, as has been previously suggested. The method could potentially be applied on other icy satellites of Jupiter (and maybe even of Saturn) when searching for atmospheric species that are able to be detected in their shadow.

### **Future Work**

More observations of high quality are needed to thoroughly investigate potential limb anomalies on Europa, and to evaluate the method's robustness with regard to variations in the Jovian background and varying model parameters. The method could also be applied to other icy satellites orbiting the gas giants for further method development.

In future observations, the shadow should be more centred in the aperture slit to avoid edge effects and enable a more uniform analysis of its proximity, and a better background model. Other wavelengths may also be analysed, as a non-zero signal is visible also outside the Ly- $\alpha$  box in Figure 3.4. Detailed investigations of the shadow's properties, such as its shape, its structure (two- or three-dimensional) and penumbra, are needed as well, to better evaluate the underlying assumptions that are made in the study.

NASA's Europa Clipper mission is planned to launch sometime in the 2020s and will visit Europa to conduct reconnaissance. It will for instance have the capability to study potential plumes *in-situ*. More observations of e.g. Europa's shadow also increase the chances of detecting plumes and specifying their properties, which would be useful information to the NASA mission. If water plumes are shown to exist, Europa Clipper carries a suite of instruments that will then be able to characterize the phenomenon in much more detail than what is possible from Earth.

# Bibliography

- Alday, J. (2017). *Ganymede's hydrogen corona and fuv albedo from hst/stis images* (Master's thesis). KTH Royal Institute of Technology. Stockholm, Sweden. <http://www.diva-portal.org/smash/record.jsf?pid=diva2%3A1188497&dswid=6368>
- Alday, J., Roth, L., Ivchenko, N., Retherford, K. D., Becker, T. M., Molyneux, P., & Saur, J. (2017). New constraints on ganymede's hydrogen corona: Analysis of lyman- $\alpha$  emissions observed by hst/stis between 1998 and 2014. *Planetary and Space Science*, *148*, 35. <https://doi.org/10.1016/j.pss.2017.10.006>
- Anderson, J. D., Schubert, G., Jacobson, R. A., Lau, E. L., Moore, W. B., & Sjogren, W. L. (1998). Europa's differentiated internal structure: Inferences from four galileo encounters. *Science*, *281*(5385), 2019–2022. <https://doi.org/10.1126/science.281.5385.2019>
- Archinal, B. A., Acton, C. H., A'Hearn, M. F., Conrad, A., Consolmagno, G. J., Duxbury, T., Hestroffer, D., Hilton, J. L., Kirk, R. L., Klioner, S. A., McCarthy, D., Meech, K., Oberst, J., Ping, J., Seidelmann, P. K., Tholen, D. J., Thomas, P. C., & Williams, I. P. (2018). Report of the iau working group on cartographic coordinates and rotational elements: 2015. *Celestial mechanics and dynamical astronomy*, *130*(3), 1–46. <https://doi.org/10.1007/s10569-017-9805-5>
- Atreya, S., Mahaffy, P., Niemann, H., Wong, M., & Owen, T. (2003). Composition and origin of the atmosphere of jupiter—an update, and implications for the extrasolar giant planets. *Planetary and Space Science*, *51*(2), 105–112. [https://doi.org/10.1016/S0032-0633\(02\)00144-7](https://doi.org/10.1016/S0032-0633(02)00144-7)
- Atreya, S., Wong, M., Owen, T., Mahaffy, P., Niemann, H., de Pater, I., Drossart, P., & Encrenaz, T. (1999). A comparison of the atmospheres of jupiter and saturn: Deep atmospheric composition, cloud structure, vertical mixing, and origin. *Planetary and Space Science*, *47*(10), 1243–1262. [https://doi.org/10.1016/S0032-0633\(99\)00047-1](https://doi.org/10.1016/S0032-0633(99)00047-1)
- Ben Jaffel, L., Kim, Y., & Clarke, J. (2007). The h lyman- $\alpha$  emission line from the upper atmosphere of jupiter: Parametric radiative transfer study and comparison with data. *Icarus*, *190*(2), 504–527. <https://doi.org/10.1016/j.icarus.2007.03.013>
- Brown, M. E. (2001). Potassium in europa's atmosphere. *Icarus*, *151*(2), 190–195. <https://doi.org/10.1006/icar.2001.6612>
- Brown, M. E., & Hill, R. E. (1996). Discovery of an extended sodium atmosphere around europa. *Nature*, *380*(6571), 229–231. <https://doi.org/10.1038/380229a0>

- Camprubí, E., de Leeuw, J. W., House, C. H., Raulin, F., Russell, M. J., Spang, A., Tirumalai, M. R., & Westall, F. (2019). The emergence of life. *Space science reviews*, 215(8), 56. <https://doi.org/10.1007/s11214-019-0624-8>
- Carr, M. H., Belton, M. J. S., Clark, R. C., Merton, E. D., Geissler, P., Greenberg, R., McEwen, A. S., Tufts, B. R., Greeley, R., Sullivan, R., Head, J. W., Pappalardo, R. T., Klaasen, K. P., Johnson, T. V., Kaufman, J., Senske, D., Moore, J., Neukum, G., Schubert, G., ... Veverka, J. (1998). Evidence for a subsurface ocean on europa. *Nature*, 391(6665), 363–365. <https://doi.org/10.1038/34857>
- Cassidy, T., Johnson, R., McGrath, M., Wong, M., & Cooper, J. (2007). The spatial morphology of europa's near-surface o<sub>2</sub> atmosphere. *Icarus (New York, N.Y. 1962)*, 191(2), 755–764. <https://doi.org/10.1016/j.icarus.2007.04.033>
- Cassidy, T., Johnson, R., & Tucker, O. (2009). Trace constituents of europa's atmosphere. *Icarus*, 201(1), 182–190. <https://doi.org/10.1016/j.icarus.2008.12.033>
- Clarke, J. T., & Gladstone, G. R. (1990). The center to limb variation in jupiter's h ly  $\alpha$  emission. *Journal of Geophysical Research: Space Physics*, 95(A12), 21281–21284. <https://doi.org/10.1029/JA095iA12p21281>
- Clarke, J. T., Gladstone, G. R., & Ben Jaffel, L. (1991). Jupiter's dayglow h ly  $\alpha$  emission line profile. *Geophysical Research Letters*, 18(11), 1935–1938. <https://doi.org/10.1029/91GL02091>
- Clarke, J. T., Weaver, H. A., Feldman, P. D., Moos, H. W., Fastie, W. G., & Opal, C. B. (1980). Spatial imaging of hydrogen lyman-alpha emission from jupiter. *The Astrophysical Journal*, 240, 696–701. <http://adsabs.harvard.edu/full/1980ApJ...240..696C>
- Dessler, A., Sandel, B., & Atreya, S. (1981). The jovian hydrogen bulge: Evidence for co-rotating magnetospheric convection. *Planetary and Space Science*, 29(2), 215–224. [https://doi.org/10.1016/0032-0633\(81\)90035-0](https://doi.org/10.1016/0032-0633(81)90035-0)
- Fagents, S. A. (2003). Considerations for effusive cryovolcanism on europa: The post-galileo perspective. *Journal of Geophysical Research - Planets*, 108(E12), 5139–n/a. <https://doi.org/10.1029/2003JE002128>
- Fagents, S. A., Greeley, R., Sullivan, R. J., Pappalardo, R. T., Prockter, L. M., & Team, T. G. S. (2000). Cryomagmatic mechanisms for the formation of rhadamanthys linea, triple band margins, and other low-albedo features on europa. *Icarus*, 144(1), 54–88. <https://doi.org/10.1006/icar.1999.6254>
- Geissler, P. E., Greenberg, R., Hoppa, G., Helfenstein, P., McEwen, A., Pappalardo, R., Tufts, R., Ockert-Bell, M., Sullivan, R., Greeley, R., Belton, M. J. S., Denk, T., Clark, B., Burns, J., Veverka, J., & the Galileo Imaging Team. (1998). Evidence for non-synchronous rotation of europa. *Nature*, 391(6665), 368–370. <https://doi.org/10.1038/34869>
- Giono, G., Roth, L., Ivchenko, N., Saur, J., Retherford, K. D., Schlegel, S., Ackland, M., & Strobel, D. F. (2020). An analysis of the statistics and systematics of limb anomaly detections in hst/stis transit images of europa. *The Astronomical Journal*, 159:155(4). <https://doi.org/10.3847/1538-3881/ab7454>

- Gladstone, G. R., Allen, M., & Yung, Y. L. (1996). Hydrocarbon photochemistry in the upper atmosphere of jupiter. *Icarus*, *119*(1), 1–52. <https://doi.org/10.1006/icar.1996.0001>
- Gladstone, G. R., Pryor, W. R., Tobiska, W. K., Stewart, A. I. F., Simmons, K. E., & Ajello, J. M. (2004). Constraints on jupiter’s hydrogen corona from galileo uvs observations. *Planetary and space science*, *52*(5-6), 415–421. <https://doi.org/10.1016/j.pss.2003.06.012>
- Greeley, D., Chyba, C. F., Head, J. W. I., McCord, T. B., McKinnon, W. B., Pappalardo, R. T., & P, F. (2004). Geology of europa. In F. Banegal, T. E. Dowling, & W. B. McKinnon (Eds.), *Jupiter: The planet, satellites and magnetosphere*. Cambridge University Press.
- Hall, D. T., Feldman, P. D., McGrath, M. A., & Strobel, D. F. (1998). The far-ultraviolet oxygen airglow of europa and ganymede. *The Astrophysical Journal*, *499*(1), 475–481. <https://doi.org/10.1086/305604>
- Hall, D. T., Strobel, D. F., Feldman, P. D., McGrath, M. A., & Weaver, H. A. (1995). Detection of an oxygen atmosphere on jupiter’s moon europa. *Nature*, *373*(6516), 677–679. <https://doi.org/10.1038/373677a0>
- Hansen, C. J., Shemansky, D. E., & Hendrix, A. (2005). Cassini uvis observations of europa’s oxygen atmosphere and torus. *Icarus*, *176*(2), 305–315. <https://doi.org/10.1016/j.icarus.2005.02.007>
- Hunten, D., Roach, F., & Chamberlain, J. (1956). A photometric unit for the airglow and aurora. *Journal of Atmospheric and Terrestrial Physics*, *8*(6), 345–346. [https://doi.org/10.1016/0021-9169\(56\)90111-8](https://doi.org/10.1016/0021-9169(56)90111-8)
- Jia, X., Kivelson, M. G., Khurana, K. K., & Kurth, W. S. (2018). Evidence of a plume on europa from galileo magnetic and plasma wave signatures. *Nature Astronomy*, *2*(6), 459–464. <https://doi.org/10.1038/s41550-018-0450-z>
- Kattenhorn, S. A., & Prockter, L. M. (2014). Evidence for subduction in the ice shell of europa. *Nature geoscience*, *7*(10), 762–767. <https://doi.org/10.1038/ngeo2245>
- Khurana, K. K., Kivelson, M. G., Stevenson, D. J., Schubert, G., Russell, C. T., Walker, R. J., & Polanskey, C. (1998). Induced magnetic fields as evidence for subsurface oceans in europa and callisto. *Nature*, *395*(6704), 777–780. <https://doi.org/10.1038/27394>
- Kivelson, M. G., Khurana, K. K., Russell, C. T., Volwerk, M., Walker, R. J., & Zimmer, C. (2000). Galileo magnetometer measurements: A stronger case for a subsurface ocean at europa. *Science*, *289*(5483), 1340–1343. <https://doi.org/10.1126/science.289.5483.1340>
- Krist, J. E., Hook, R. N., & Stoehr, F. (2011). 20 years of hubble space telescope optical modeling using tiny tim. <https://doi.org/10.1117/12.892762>
- Lagarias, J. C., Reeds, J. A., Wright, M. H., & Wright, P. E. (1998). Convergence properties of the nelder–mead simplex method in low dimensions. *SIAM journal on optimization*, *9*(1), 112–147. <https://doi.org/10.1137/s1052623496303470>
- LASP. (2020). *Composite solar lyman-alpha, time series* (U. of Colorado Boulder, Ed.). Retrieved June 3, 2020, from [https://lasp.colorado.edu/lisird/data/composite\\_lyman\\_alpha/](https://lasp.colorado.edu/lisird/data/composite_lyman_alpha/)

- Lesage, E., Massol, H., & Schmidt, F. (2020). Cryomagma ascent on europa. *Icarus*, *335*, 113369. <https://doi.org/10.1016/j.icarus.2019.07.003>
- Manga, M., & Wang, C.-Y. (2007). Pressurized oceans and the eruption of liquid water on europa and enceladus. *Geophysical Research Letters*, *34*(7), L07202–n/a. <https://doi.org/10.1029/2007GL029297>
- Mauk, B. H., Mitchell, D. G., Krimigis, S. M., Roelof, E. C., & Paranicas, C. P. (2003). Energetic neutral atoms from a trans-europa gas torus at jupiter. *Nature (London)*, *421*(6926), 920–922. <https://doi.org/10.1038/nature01431>
- Melin, H., & Stallard, T. (2016). Jupiter’s hydrogen bulge: A cassini perspective. *Icarus*, *278*, 238–247. <https://doi.org/10.1016/j.icarus.2016.06.023>
- Misra, D., Mishra, S., & Appasani, B. (2018). Advanced image processing for astronomical images. <https://arxiv.org/abs/1812.09702>
- Mitri, G., & Showman, A. P. (2008). A model for the temperature-dependence of tidal dissipation in convective plumes on icy satellites: Implications for europa and enceladus. *Icarus*, *195*(2), 758–764. <https://doi.org/10.1016/j.icarus.2008.01.010>
- Moses, J. I., Fouchet, T., Yelle, R. V., Friedson, A. J., Orton, G. S., Bézard, B., Drossart, P., Gladstone, G. R., Kostiuk, T., & Livengood, T. A. (2004). The stratosphere of jupiter. In F. Banegal, T. E. Dowling, & W. B. McKinnon (Eds.), *Jupiter: The planet, satellites and magnetosphere*. Cambridge University Press.
- Neveu, M., Desch, S., Shock, E., & Glein, C. (2015). Prerequisites for explosive cryovolcanism on dwarf planet-class kuiper belt objects. *Icarus*, *246*, 48–64. <https://doi.org/10.1016/j.icarus.2014.03.043>
- Nimmo, F., & Porco, C. (2014). Chapter 39 - enceladus. In T. Spohn, D. Breuer, & T. V. Johnson (Eds.), *Encyclopedia of the solar system* (Third Edition, pp. 851–859). Elsevier Inc. <https://doi.org/10.1016/B978-0-12-415845-0.00039-6>
- Noviello, J., Torrano, Z., Rhoden, A., & Singer, K. (2019). Mapping europa’s microfeatures in regional mosaics: New constraints on formation models. *Icarus*, *329*, 101–123. <https://doi.org/10.1016/j.icarus.2019.02.038>
- Paganini, L., Villanueva, G. L., Roth, L., Mandell, A. M., Hurford, T. A., Retherford, K. D., & Mumma, M. J. (2020). A measurement of water vapour amid a largely quiescent environment on europa. *Nature Astronomy*, *4*(3), 266–272. <https://doi.org/10.1038/s41550-019-0933-6>
- Pappalardo, R. T. (2013). Jupiter’s water worlds: Water lurks beneath the surfaces of europa, ganymede, and callisto. In M. Carroll & R. Lopes (Eds.), *Alien seas: Oceans in space* (2013th ed.). New York, NY, Springer. [https://doi.org/10.1007/978-1-4614-7473-9\\_5](https://doi.org/10.1007/978-1-4614-7473-9_5)
- Pappalardo, R. T., Belton, M. J. S., Breneman, H. H., Carr, M. H., Chapman, C. R., Collins, G. C., Denk, T., Fagents, S., Geissler, P. E., Giese, B., Greeley, R., Greenberg, R., Head, J. W., Helfenstein, P., Hoppa, G., Kadel, S. D., Klaasen, K. P., Klemaszewski, J. E., Magee, K., ... Williams, K. K. (1999). Does europa have a subsurface ocean? evaluation of the geological evidence. *Journal of Geophysical Research: Planets*, *104*(E10), 24015–24055. <https://doi.org/10.1029/1998JE000628>

- Prockter, L. M., & Pappalardo, R. T. (2014). Chapter 36 - europa. In T. Spohn, D. Breuer, & T. V. Johnson (Eds.), *Encyclopedia of the solar system* (Third Edition, pp. 793–811). Elsevier Inc. <https://doi.org/10.1016/B978-0-12-415845-0.00036-0>
- Quick, L. C., Barnouin, O. S., Prockter, L. M., & Patterson, G. W. (2013). Constraints on the detection of cryovolcanic plumes on europa. *Planetary and Space Science*, *86*, 1–9. <https://doi.org/10.1016/j.pss.2013.06.028>
- Riley, A., & the STIS Team. (2019). *Stis instrument handbook*. Baltimore: STScI.
- Roth, L., Retherford, K. D., Ivchenko, N., Schlatter, N., Strobel, D. F., Becker, T. M., & Grava, C. (2017). Detection of a hydrogen corona in hst ly $\alpha$  images of europa in transit of jupiter. *The Astronomical Journal*, *153*:67(2). <https://doi.org/10.3847/1538-3881/153/2/67>
- Roth, L., Retherford, K. D., Saur, J., Strobel, D. F., Feldman, P. D., McGrath, M. A., & Nimmo, F. (2014a). Orbital apocenter is not a sufficient condition for hst/stis detection of europa’s water vapor aurora. *Proceedings of the National Academy of Sciences - PNAS*, *111*(48), E5123. <https://doi.org/10.1073/pnas.1416671111>
- Roth, L., Saur, J., Retherford, K. D., Strobel, D. F., Feldman, P. D., McGrath, M. A., & Nimmo, F. (2014b). Transient water vapor at europa’s south pole. *Science*, *343*(6167), 171–174. <https://doi.org/10.1126/science.1247051>
- Roth, L., Saur, J., Retherford, K. D., Strobel, D. F., Feldman, P. D., McGrath, M. A., Spencer, J. R., Blöcker, A., & Ivchenko, N. (2016). Europa’s far ultraviolet oxygen aurora from a comprehensive set of hst observations. *Journal of geophysical research. Space physics*, *121*(3), 2143–2170. <https://doi.org/10.1002/2015JA022073>
- Roth, L. [Lorenz]. (2012). *Aurorae of io and europa: Observations and modeling* (Doctoral dissertation). University of Cologne. Cologne, Germany.
- Russell, M. J., Murray, A. E., & Hand, K. P. (2017). The possible emergence of life and differentiation of a shallow biosphere on irradiated icy worlds: The example of europa. *Astrobiology*, *17*(12), 1265–1273. <https://doi.org/10.1089/ast.2016.1600>
- Sandel, B. R., Broadfoot, A. L., & Strobel, D. F. (1980). Discovery of a longitudinal asymmetry in the h lyman-alpha brightness of jupiter. *Geophysical Research Letters*, *7*(1), 5–8. <https://doi.org/10.1029/GL007i001p00005>
- Schubert, G., Anderson, J. D., Spohn, T., & McKinnon, W. B. (2004). Interior composition, structure and dynamics of the galilean satellites. In F. Banegal, T. E. Dowling, & W. B. McKinnon (Eds.), *Jupiter: The planet, satellites and magnetosphere*. Cambridge University Press.
- Shematovich, V., Johnson, R., Cooper, J., & Wong, M. (2005). Surface-bounded atmosphere of europa. *Icarus*, *173*(2), 480–498. <https://doi.org/10.1016/j.icarus.2004.08.013>
- Sheppard, S. S. (2018). *A dozen new moons of jupiter discovered, including one “oddball”*. Retrieved July 1, 2020, from <https://carnegiescience.edu/news/dozen-new-moons-jupiter-discovered-including-one-%E2%80%9Coddball%E2%80%9D>
- Skinner, T. E., Deland, M. T., Ballester, G. E., Coplin, K. A., Feldman, P. D., & Moos, H. W. (1988). Temporal variation of the jovian h i lyman alpha emission (1979-

- 1986). *Journal of Geophysical Research: Space Physics*, 93(A1), 29–34. <https://doi.org/10.1029/JA093iA01p00029>
- Smith, H. T., Mitchell, D. G., Johnson, R. E., Mauk, B. H., & Smith, J. E. (2019). Europa neutral torus confirmation and characterization based on observations and modeling. *The Astrophysical Journal*, 871(1), 69. <https://doi.org/10.3847/1538-4357/aaed38>
- Smyth, W. H., & Marconi, M. L. (2006). Europa's atmosphere, gas tori, and magnetospheric implications. *Icarus*, 181(2), 510–526. <https://doi.org/10.1016/j.icarus.2005.10.019>
- Sohn, S. T., & the STIS Team. (2019). *Stis data handbook*. Baltimore: STScI.
- Sparks, W. B., Hand, K. P., McGrath, M. A., Bergeron, E., Cracraft, M., & Deustua, S. E. (2016). Probing for evidence of plumes on europa with hst/stis. *The Astrophysical Journal*, 829(2), 121. <https://doi.org/10.3847/0004-637X/829/2/121>
- Sparks, W. B., Schmidt, B. E., McGrath, M. A., Hand, K. P., Spencer, J. R., Cracraft, M., & Deustua, S. E. (2017). Active cryovolcanism on europa? *Astrophysical Journal Letters*, 839(2), L18. <https://doi.org/10.3847/2041-8213/aa67f8>
- Starck, J.-L., & Murtagh, F. (2006). *Astronomical image and data analysis* (2nd ed.). Berlin, Heidelberg, Springer.
- West, R. A. (2014). Chapter 32 - atmospheres of the giant planets. In T. Spohn, D. Breuer, & T. V. Johnson (Eds.), *Encyclopedia of the solar system* (Third Edition, pp. 723–742). Elsevier Inc. <https://doi.org/10.1016/B978-0-12-415845-0.00032-3>
- Yelle, R. V., & Miller, S. (2004). Jupiter's thermosphere and ionosphere. In F. Banegal, T. E. Dowling, & W. B. McKinnon (Eds.), *Jupiter: The planet, satellites and magnetosphere*. Cambridge University Press.
- Yoshino, K., Esmond, J., Parkinson, W., Ito, K., & Matsui, T. (1996). Absorption cross section measurements of water vapor in the wavelength region 120 to 188 nm. *Chemical Physics*, 211(1), 387–391. [https://doi.org/10.1016/0301-0104\(96\)00210-8](https://doi.org/10.1016/0301-0104(96)00210-8)
- Zimmer, C., Khurana, K. K., & Kivelson, M. G. (2000). Subsurface oceans on europa and callisto: Constraints from galileo magnetometer observations. *Icarus*, 147(2), 329–347. <https://doi.org/10.1006/icar.2000.6456>

# Appendix A

## Calculation of the Shadow Penumbra

A model for Europa's shadow with an included penumbra is presented here. Figure A.1 illustrates how the umbra and penumbra are generated by the occultation geometry of the Sun, Europa, and Jupiter. A simplified model is used, where the objects are represented as planar disks that are all parallel. The purpose is to calculate the shadow's umbra and penumbra diameters, from which a linear profile is fitted between their borders.

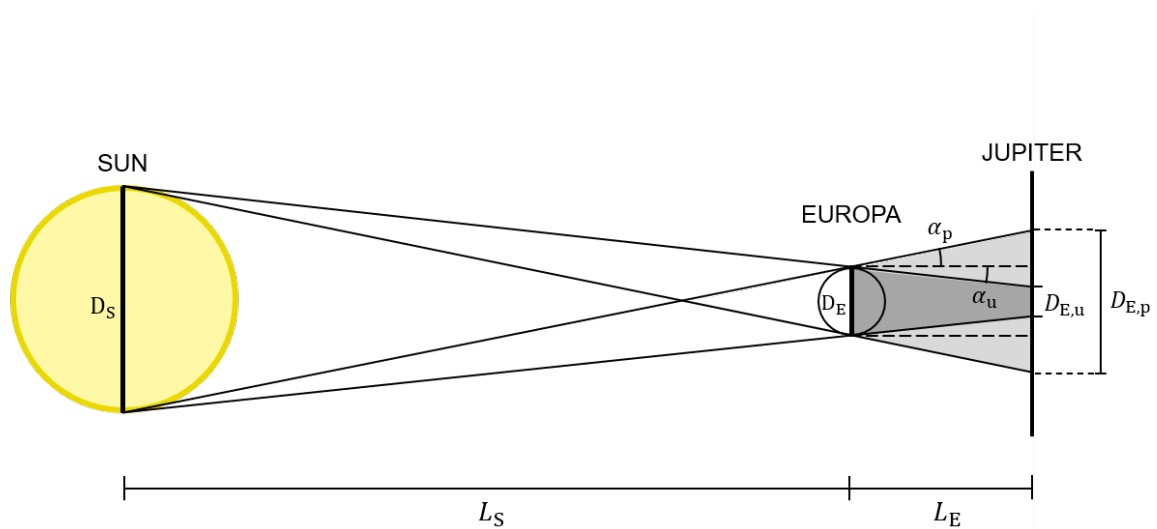


**Figure A.1:** Not to scale geometry of the Sun-Europa-Jupiter occultation (as viewed in profile).  $L_S$  is the distance between the Sun and Europa and  $L_E$  is the distance between Europa and Jupiter.  $D_S$  is the Sun's diameter,  $D_E$  is Europa's diameter,  $D_{E,u}$  is the diameter of the shadow's umbra (dark grey), and  $D_{E,p}$  is the diameter of the shadow's penumbra (light grey). The umbra angle,  $\alpha_u$ , and penumbra angle,  $\alpha_p$ , together span the penumbra after the light passes Europa.

The umbra ( $\alpha_u$ ) and penumbra ( $\alpha_p$ ) angles are computed as

$$\alpha_u = \arcsin\left(\frac{D_S - D_E}{2L_S}\right), \quad \alpha_p = \arcsin\left(\frac{D_S + D_E}{2L_S}\right), \quad (\text{A.1})$$

where  $D_S$  is the Sun's diameter (the extended light source),  $D_E$  is Europa's diameter (the obscuring body) and  $L_S$  is the distance between the Sun and Europa. The umbra's diameter decrease can then be approximated as  $\alpha_u \cdot L_E$ , and the penumbra's diameter increase as  $\alpha_p \cdot L_E$ . The umbra ( $D_{E,u}$ ) and penumbra ( $D_{E,p}$ ) diameters are finally given as

$$D_{E,u} = D_E - (2\alpha_u L_E), \quad D_{E,p} = D_E + (2\alpha_p L_E), \quad (\text{A.2})$$

where the distance  $L_E$  is between Europa and Jupiter's H scattering corona (assumed as the  $1 R_J$  surface).

From the Jovian surface the Sun and Europa look like two circular disks, where the Sun is occulted by Europa. This geometry produces a non-linear increase in brightness of the Jovian dayglow from umbra to penumbra. A simplification is therefore made, as visible in Figure A.2, where the light source and obscuring body are square, which creates a linear brightness profile in the penumbra. The complete simplified model is displayed in an example radial profile in Figure A.3.

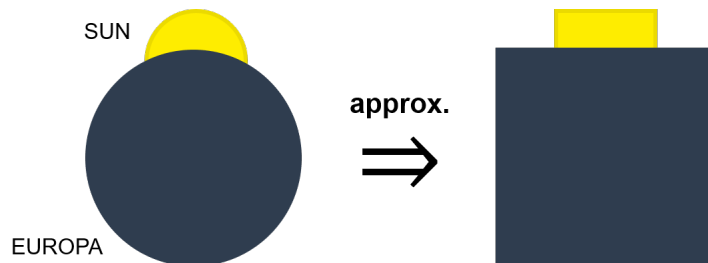


**Figure A.2:** *Simplification of the Sun's and Europa's disk geometries. Both light source and obscuring body are approximated as squares, to have a linear brightness profile in the penumbra.*

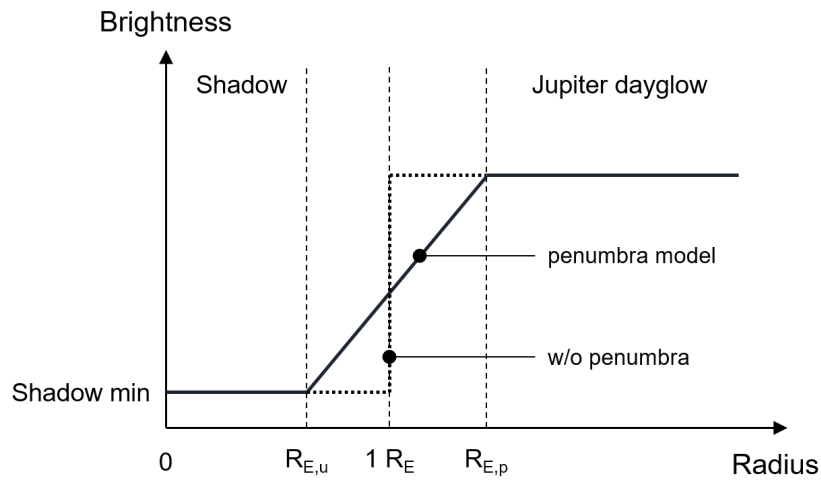


**Figure A.3:** Radial profile of the simplified penumbra model (solid line). The radii  $R_{E,u}$  and  $R_{E,p}$  are of the umbra and penumbra respectively. A shadow profile without a penumbra (dotted line) is displayed as reference.

# Appendix B

## Radial Profile Bins

The concentric rings that make up the bins for the radial profiles are displayed in Figure B.1. The bins are  $0.1 R_E$  wide in the radial direction. The enclosed area that is used for sampling the image (white dashed line) shows how the radial bins are asymmetrically cut off in  $x$  and  $y$ , which creates a dip in the resulting profiles, as visible in Figure 4.2.

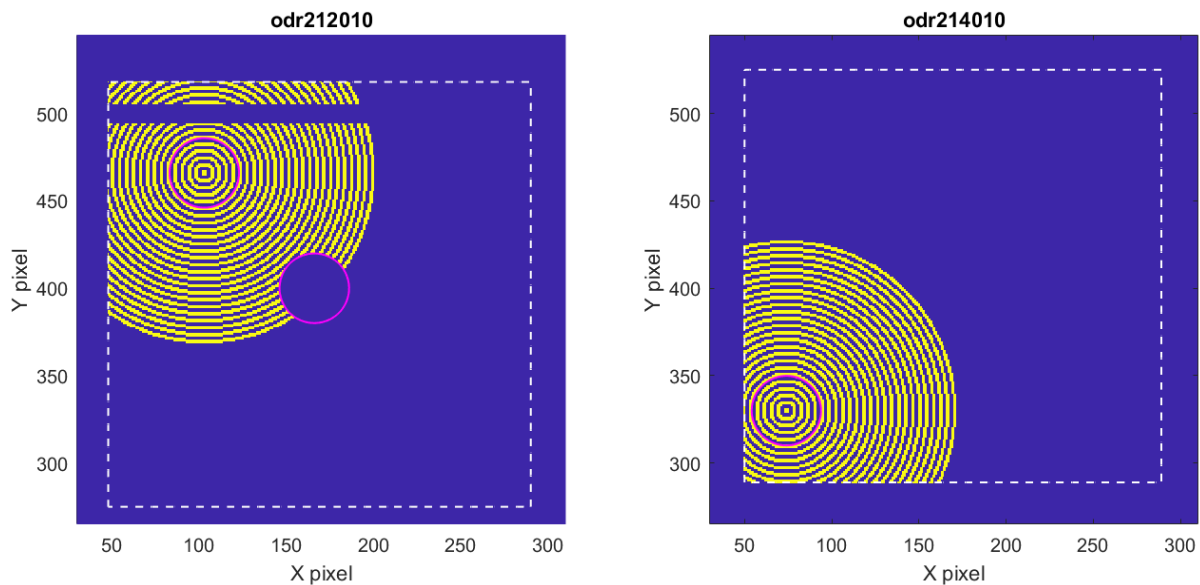


**Figure B.1:** Radial profile bins for odr212010 (left panel) and odr214010 (right panel). Every other bin is marked in yellow to illustrate their concentric ring-shape. The magenta circles indicate the moon and shadow disks, where the moon in odr212010 is excluded from the pixel sampling, as well as the MAMA detector's repeller wire at  $y \approx 500$  pixels. The white dashed boxes indicate the enclosed area that is used for sampling the image throughout the image analysis.

# Appendix C

## Excluded Areas for Odr212010 Background Fit

Figure C.1 displays the image of odr212010, with the areas that are excluded from the background surface fit. Europa, its shadow and the repeller wire are excluded, and the image is bounded to only included pixels within the Ly- $\alpha$  aperture box.

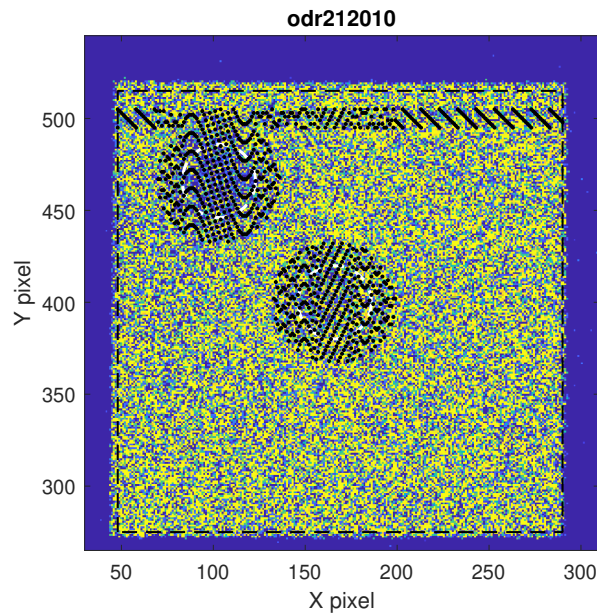


**Figure C.1:** Areas excluded from the odr212010 background surface fit, shown as regions of black dots. Europa, its shadow and the repeller wire are excluded. The black dashed box restricts the background fit to only include pixels within the Ly- $\alpha$  aperture box.



